Laser cavity-soliton microcombs

Article (Accepted Version)

Laser Cavity-Soliton Micro-Combs

Hualong Bao[1], Andrew Cooper[1], Maxwell Rowley[1], Luigi Di Lauro[1], Juan Sebastian Totero Gongora[1], Sai T. Chu[2], Brent E. Little[3], Gian-Luca Oppo[4], Roberto Morandotti[5,6,7], David J. Moss[8], Benjamin Wetzel[1], Marco Peccianti[1] and Alessia Pasquazi[1*]

[1]*Emergent Photonics (Epic) Lab, Dept. of Physics and Astronomy, University of Sussex, BN1 9QH, UK*
[2]*Department of Physics, City University of Hong Kong, Tat Chee Avenue, Hong Kong, China SAR*
[3]*State Key Laboratory of Transient Optics and Photonics, Xi'an Institute of Optics and Precision Mechanics, CAS, Xi'an, China*
[4]*SUPA, Department of Physics, University of Strathclyde, Glasgow, United Kingdom*
[5]*INRS-EMT, 1650 Boulevard Lionel-Boulet, Varennes, Québec, Canada J3X 1S2*
[6]*Institute of Fundamental and Frontier Sciences, University of Electronic Science and Technology of China, Chengdu 610054, Sichuan, China*
[7]*ITMO University, St. Petersburg 199034, Russia*
[8]*Centre for Microphotonics, Swinburne University of Technology, Hawthorn, VIC 3122, Australia*

**Corresponding author: a.pasquazi@sussex.ac.uk*

Micro-cavity based frequency combs, or 'micro-combs' [1,2], have enabled many fundamental breakthroughs [3-21] through the discovery of temporal cavity-solitons. These self-localised waves, described by the Lugiato-Lefever equation [22], are sustained by a background of radiation usually containing 95% of the power [23]. Simple methods for their efficient generation and control are currently being investigated to finally establish micro-combs as out-of-the-lab tools [24].

Here, we demonstrate *micro-comb laser* cavity-solitons. Laser cavity-solitons are intrinsically background free and have underpinned key breakthroughs in semiconductor lasers [22,25-28]. By merging their properties with the physics of multi-mode systems [29], we provide a new paradigm for soliton generation and control in micro-cavities. We demonstrate 50 nm wide bright soliton combs induced at average powers more than *one order of magnitude* lower than the Lugiato-Lefever soliton power threshold [22], measuring a mode efficiency of 75% versus the theoretical limit of 5% for bright Lugiato-Lefever solitons [23]. Finally, we can tune the repetition-rate by well over a megahertz without any active feedback.

Optical frequency combs based on micro-cavity resonators, also called 'micro-combs', offer the promise of achieving the full capability of their bulk counterparts, yet in an integrated footprint [1, 2]. They have enabled major breakthroughs in spectroscopy [3,4], communications [5,6] microwave photonics [7], frequency synthesis [8], optical ranging [9,10], quantum sources [11, 12], metrology [13,14] and astrocombs [15,16].

Of particular importance has been the discovery of temporal cavity-solitons in micro-cavities [17-21]. Temporal cavity-solitons [2,17-23] are an important example of dissipative solitons – self-confined waves balancing dispersion with the nonlinear phase-shift in lossy systems [30]. Practical applications of these pulses for micro-combs, however, still face significant challenges. In particular, they achieve a limited *mode efficiency*, defined as the fraction of optical power residing in the comb modes other than the most powerful one. Solitons in micro-cavities exist as localised states upon a background, usually a continuous-wave (CW) [2,17-23], which results in a dominant mode in the comb spectrum. In this configuration, described by the

well-known Lugiato-Lefever equation, bright solitons have a mode efficiency theoretically bounded to 5% [23], limiting the efficiency of state-of-the-art micro-combs based on this operating principle [2,23-24,31].

Furthermore, controlling their fundamental parameters, such as repetition-rate, has posed a challenge. Currently, tuning their repetition-rate requires either complex methods involving fast detection, microwave signal processing and fast cavity actuation, or novel approaches such as pulsed [16,32] or counter-propagating [33] pumping, or heterodyning with coupled micro-resonators [34]. Finding a solution to these fundamental issues has attracted significant effort [24, 31].

Here, we demonstrate a distinct class of solitary pulses in micro-combs – temporal ***laser*** cavity-solitons – that directly addresses these challenges. Laser cavity-solitons [22,25-28] have been largely studied in spatial configurations such as semiconductor lasers [25], where they enabled breakthroughs such as all-optical reconfigurable memories [26]. More recently, they have been observed in both temporal [28] and spatio-temporal [35] contexts. They are fundamentally different to externally driven cavity-solitons, which are sustained by the energy of the pumping background. Laser cavity-solitons, in contrast, receive energy directly from the gain of the lasing medium. As result, they exist without any background light and are intrinsically the most energy efficient class of cavity-solitons.

By nesting a Kerr micro-resonator in a fibre loop with gain, we harvest the intrinsic capability of laser cavity-solitons, demonstrating that they can be used to achieve highly efficient, broadband micro-comb generation. We excite bright solitons having a bandwidth of more than 50 nm, using average powers less than ***6% of the threshold*** for Lugiato-Lefever solitons in an equivalent resonator. Our background-free solitons have a *mode efficiency* of 75%, with a theoretical maximum predicted to be 96%. Furthermore, by exploring the properties of multi-mode systems, recently investigated for spatio-temporal mode-locking [29] and spatial beam self-cleaning [36], we show that the repetition-rate of our pulses can be adjusted by reconfiguring simple parameters such as the laser cavity-length. Without the use of active control, we succeed in modifying their repetition-rate by more than a megahertz.

The principle of operation is shown in Fig. 1a. A nonlinear micro-cavity (cavity 'a') is embedded within a longer amplifying fibre cavity (cavity 'b'). The pulse propagating in the fibre loop, spectrally limited by the laser-gain bandwidth, sustains in the micro-cavity the existence of a pulse which is broadened by the Kerr nonlinearity over the gain bandwidth [25,37]. This architecture is inspired by the concept of a filter-driven four-wave mixing laser [38]. Our present analysis allows us to define the solitary state existence and understand the nature of previous observations [2,38,39]. In particular, we show that the relative position of the oscillating modes within the micro-cavity resonances is critical to realise this new class of broadband solitary pulses.

Temporal cavity-solitons can be effectively modelled using mean-field approaches, such as the Lugiato-Lefever equation [17], where the field in the micro-cavity is described as a pulse propagating in time, along with a spatial coordinate periodically looped within the micro-resonator length. Here, we build a set of multi-component (or 'vectorial') laser mean-field equations [29,36] by coupling together the micro-cavity field with the main-cavity 'super-mode' fields. (Supplementary/Methods). A super-mode is an optical radiation formed by a set of equally-spaced modes of the main-cavity, whose relative spacing (in frequency) is set by the micro-cavity free-spectral range (FSR) F_a. Quantitively, the mth resonance $f_m^{(b)}$ of a super-mode can be linked to the micro-cavity resonances $f_m^{(a)}$ by the relation

$$f_m^{(b)} = f_m^{(a)} - (\Delta - q - m\,\delta)\,F_b, \tag{1}$$

where F_b is the main-cavity FSR and q is an integer defining the order of the super-mode (see Fig. 1b). In general, the q-order super-mode is frequency detuned with respect to the micro-cavity resonance by $(\Delta - q)\,F_b$, where Δ is the cavity-frequency offset, normalised against F_b. The key features of the laser are determined by the leading-order super-mode, defined for $q = 0$, which possesses the largest spectral

overlap with the micro-cavity resonances. Higher-order super-modes ($q \neq 0$) typically experience greater coupling losses. Because F_b is not necessarily an integer divisor of F_a, we introduce the variable δ, normalised against F_b, representing the FSR detuning.

Two numerical examples of linear and solitary propagation are reported in Fig. 2. We use a spatial coordinate periodically closed over the micro-cavity length because the temporal waveform of every super-mode is periodic with the micro-cavity round-trip time T_a, with a period slightly detuned by δ (Eq. (1)). The parameters $\Delta - q$ and δ play the role of the frequency and group velocity mismatches between the micro-cavity and super-mode fields. A key property of solitary waves in vectorial equations, also recently shown for spatio-temporal mode-locking [29], is that all the coupled fields *lock* to a single group velocity (or repetition-rate detuning) v (Fig. 2a and b) and carrier frequency offset ϕ (Fig. 2c, see also model Equations in the Methods). Practically, the system provides a well-defined soliton comb, with the n^{th} frequency tooth $f_n^{(S)}$ expressed as

$$f_n^{(S)} = f_n^{(a)} + (\phi - n\, v)\, F_b. \tag{2}$$

The parameters ϕ and v are selected by Δ and δ, together with the normalised saturated gain g (Methods/Supplementary).

The measurements of laser cavity soliton micro-combs at different intra-cavity powers are in Fig. 3a-f. The spectra exhibit a bandwidth of up to 50 nm - comparable to the cavity-solitons observed in resonators with similar dispersion properties [9,20,21] - and, together with the corresponding autocorrelations (Fig. 3a, c, e and inset), are in excellent agreement with theory.

We used intra-cavity laser-scanning spectroscopy (see Methods) (Fig. 3b, c and f) to measure the frequency of the oscillating modes and their position within the micro-cavity resonance, obtaining important insights into the solitary nature of the solution.

A bistable system can display both localised and non-localised coherent waves [22]. Solitons are localised states that can appear in groups of non-equidistant pulses, such as the triplet seen in Fig. 3e-f. The stability of their tails requires the stability of the background, which is theoretically expected for oscillating modes that are red-detuned with respect to the micro-cavity resonance (Methods, Supplementary and Fig. 4a). These facts are in excellent agreement with the measurements shown in Figs. 3b, d and f. We attribute the small, blue-detuned mode found only in the central resonance to a perturbation on the soliton tails, against which localised pulses are robust (Supplementary).

Conversely, coherent patterns are non-localised, periodic waves which fill the entire cavity. Type I [2] and type II combs in the Lugiato-Lefever system are characteristic examples of patterns that typically have a narrower bandwidth than solitons. Earlier observations, [2,38-40] limited to picosecond pulse durations and displaying Type I ([39] and Supplementary) and II [40] comb shapes, are consistent with this picture. Furthermore, laser scanning spectroscopy measurements (see Supplementary and [40]) on these types of pulses reveal blue-detuned modes, for which the theory forbids stable solitons but while allowing patterns originating from the modulational instability of the background state [22].

Our experiments demonstrate the inherently higher efficiency of our class of laser cavity-solitons compared to Lugiato-Lefever solitons that feature a dominant comb mode, located at the pump wavelength, comprising the energy of the CW background (Fig. 4b-c). For Lugiato-Lefever solitons, the mode efficiency has a theoretical limit of 5% and 50% for bright and dark solitons, respectively [23]. Our mode efficiency in the experiments of Fig. 3 is greater than 75% for bright solutions. Further, we theoretically predict a maximum mode efficiency of 96% for bright laser cavity-solitons. This contrasts with state-of-the-art devices based on bright Lugiato-Lefever solitons that have mode efficiencies on the order of 1.6% to 5% [23,31]. Lugiato-Lefever solitons feature a minimum power excitation threshold above which the Kerr

nonlinearity induces bistability, yielding the two CW states necessary for the soliton's existence (Fig.4a). Our laser cavity-solitons, in contrast, require a zero background with a single CW state and exist below the Kerr bistability threshold. By comparing experiment with theory, we find that our peak powers injected into the micro-cavity are below 50% of the input power *threshold* of a Lugiato-Lefever soliton for the same micro-resonator. Because our injected field is pulsed, the injected average power to the micro-resonator is less than 6% of this threshold power (Supplementary).

To demonstrate the capability of changing the soliton repetition-rate using simple methods, we varied the main-cavity FSR detuning δ with a delay line that modified the fibre cavity length, and hence the mode-spacing F_b. Gain and loss were also adjusted to maintain the solitary state. Fig. 5 shows the repetition-rate variations for three cases (Fig. 5a). We measured the frequency position of the comb modes against the mode number using laser-spectroscopy. We then calculated the best-fit for the first case (Comb 1) and subtracted the frequency positions for the three cases, obtaining the residual frequency versus mode number in Fig. 5b. This shows a change in repetition-rate of over a megahertz. The theoretical results (Fig.5c and Supplementary) demonstrate that, by changing δ within the experimentally achievable range, the soliton stability is maintained while its velocity is modified – thus varying the repetition rate.

Finally, we achieve these localised states by manual adjustment of the fibre cavity parameters, such as cavity length, gain current and polarisation losses, in a similar fashion to passively mode-locked lasers. This approach enables the use of powerful methods, such as genetic algorithms, that have been instrumental in achieving adaptive control of the soliton properties and self-starting operation in passive mode-locking [41].

In conclusion, we report the observation of temporal laser cavity-solitons in optical micro-combs. Our results merge the powerful physics of optical Kerr micro-combs and their ability to generate large bandwidths with the unique properties of laser cavity-solitons and multi-mode systems. In contrast to conventional coherently-driven cavity-solitons, this new class of cavity-solitons is intrinsically background free, making them extremely energy efficient. Furthermore, thanks to a tailored two-cavity configuration, crucial properties, such as the repetition-rate, can be controlled with simple elements such as a delay line. Laser-cavity solitons represent a new and powerful mode of operation for micro-combs, offering many advantages that will help pave the road towards enabling these devices to move out of the laboratory towards real-world applications.

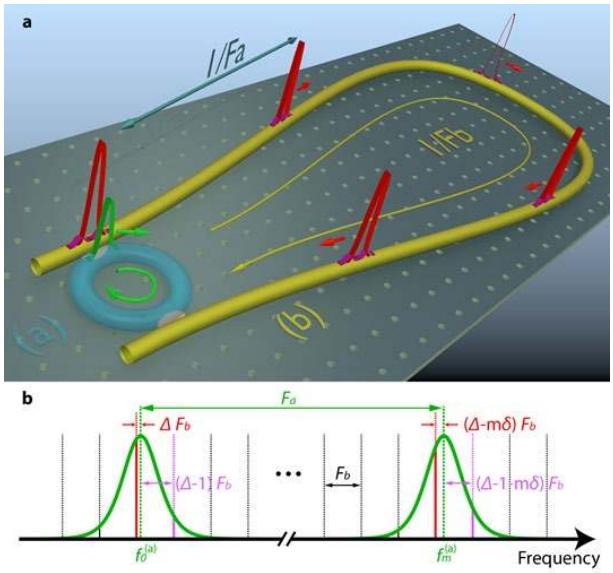

Figure 1. Principle of operation of micro-comb laser cavity-soliton formation. **a.** A short pulse (green) propagates in the micro-cavity (blue) sustained by a longer pulse (red) and a weak higher-order 'super-mode pulse' (purple) in the amplifying loop (yellow). This depicts the fundamental operation of a single soliton per cavity. **b.** Cold-cavity spectral distribution. Micro-cavity resonances are depicted in green, amplifying-cavity resonances are in black, with leading and first-order super-modes highlighted in red and purple, respectively. The normalised frequency offset between the central frequency of the leading super-mode and the micro-cavity resonance is Δ; similarly, the frequency offset is Δ-1 for the central frequency of first-order super-mode. In the convention used here and in Eq. (1), positive values of Δ correspond to a leading order super-mode red-detuned with respect to the micro-cavity resonances. The variable δ is the normalised FSR detuning, appearing when the two cavities are not commensurate.

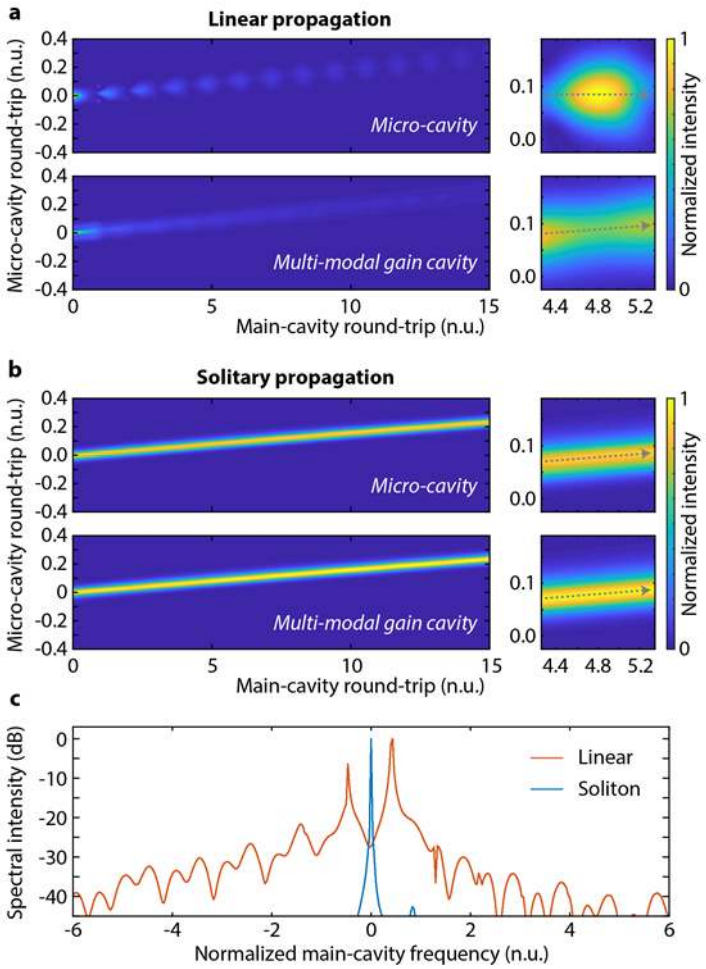

Figure 2. Theoretical propagation of linear and solitary pulses. Micro-cavity and gain cavity have a group velocity mismatch δ = 0.03. In these examples we used Δ =0.47; g= 0.14 and N=30 in Eqs. (3) and (4) in the Methods. **a.** Evolution of the micro-cavity and multi-modal amplifying-cavity fields in the linear case. The quantities in the upper and lower panels are the overall field intensities in the two cavities are $|a(t,x)|^2$ and $\sum_{-N}^{N}|b_q(t,x)|^2$, with reference to Eq. (3) and (4) in the Methods. The group velocity of the fields is better shown in the insets, where the direction of the field is marked with an arrow. The mismatch between such group velocities causes a periodical decoupling of the fields. **b.** Solitary propagation: both fields lock to the same group velocity v. **c.** Equivalent spectral distribution of the super-modes within a resonance of the micro-cavity (Supplementary). Such a spectrum, for the linear case (orange), highlights the presence of many frequency components, one for every super-mode with frequency offset $\Delta - q$. In the case of solitary propagation (blue), conversely, all the modes *lock* to the frequency ϕ.

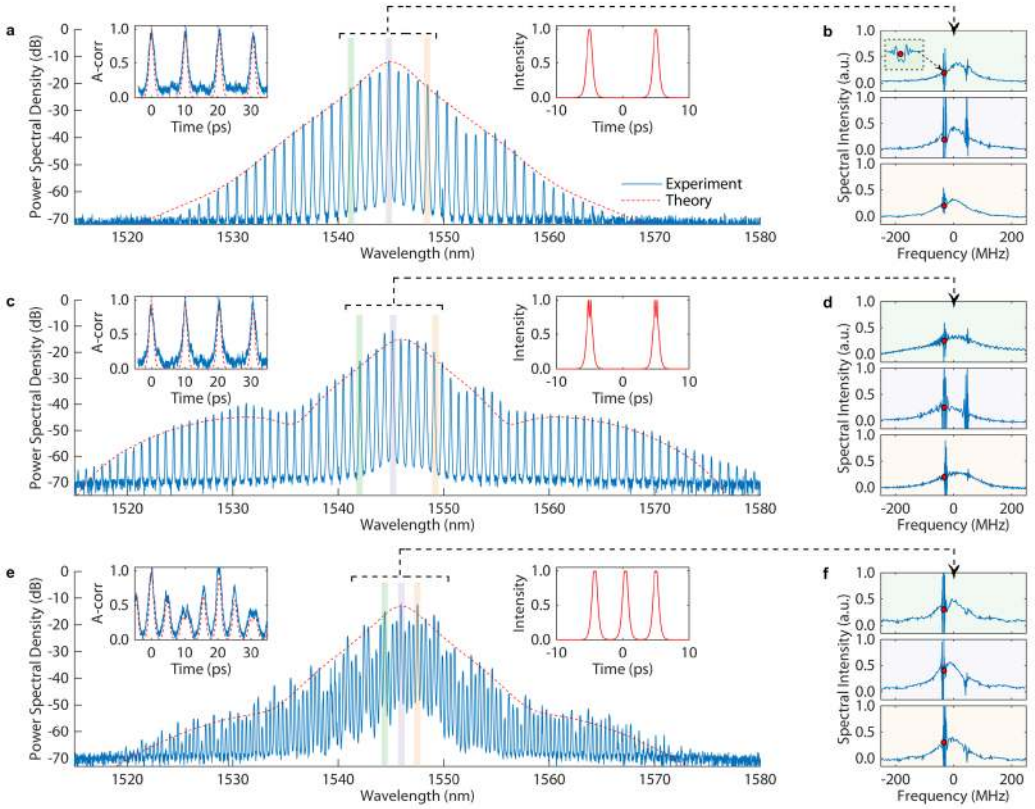

Figure 3. Temporal laser cavity-soliton measurement. a. Soliton generation, for two equidistant solitons per round-trip. Intra-cavity power at the output of the amplifier is 100 mW and at the output of the micro-cavity is 20 mW. Spectrum (in logarithmic scale) and autocorrelation (left inset). The experimental measurements (blue) are compared to the theoretical solitary state (red). Fit parameters are Δ = 0.49; g= 0.1. The theoretical normalised soliton frequency is $\phi = -0.475$, corresponding to a red-shifted frequency of 36 MHz (Eq. 2) for F_b = 77 MHz (Methods). The right inset reports the theoretical intensity profile in the micro-cavity. **b.** Intra-cavity spectrum (blue), evidencing within each micro-cavity resonance the lasing modes (red dots, red-shifted of approximately 32 MHz from the micro-cavity centre, in excellent agreement with the theory). The three plots correspond to the comb wavelengths highlighted in panel (a) by different colour shading. **c, d.** The same measurements at higher fibre gain for two equidistant solitons per round-trip, leading to 150 mW intra-cavity power at the output of the amplifier and 30 mW at the output of the ring, showing that the bandwidth of the soliton increases with the gain. Fit parameters are Δ =0.47; g= 0.14, with $\phi = -0.474$. The shape of the spectrum diverges from the sech-like, triangular shape of the case a,b. The formation of the lateral wings can be qualitatively related to a modulational instability effect on the peak of the pulse, shown in the theoretical intensity pulses in the right inset [22]. **e, f.** The same measurements for three solitons per round-trip for the same intra-cavity power of case c, d. Fit parameters are Δ = 0.49; g = 0.11, with $\phi = -0.477$. Because there is an additional soliton in the cavity, the energy per soliton is lower than the case c,d, leading to a narrower spectrum. The autocorrelation shows that the solitons are not equidistant, highlighting the localised nature of the solution.

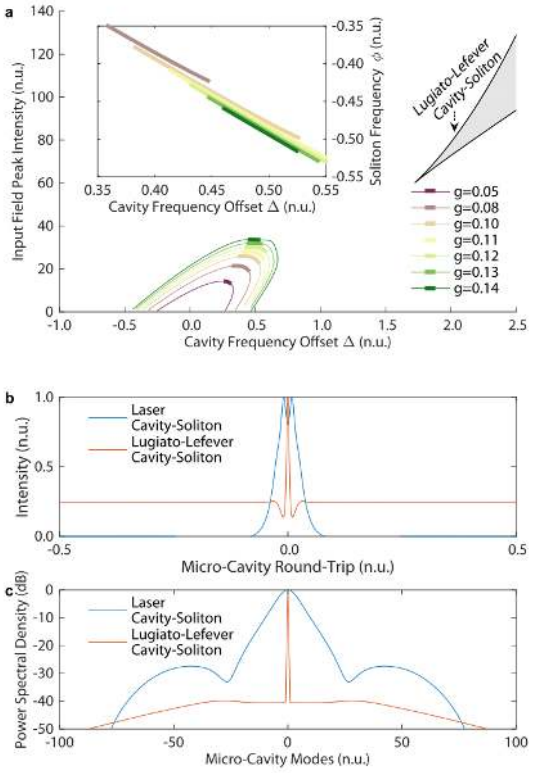

Figure 4. Temporal laser cavity-soliton and Lugiato-Lefever cavity-soliton comparison. a. Plot of laser cavity-soliton input field peak power versus normalised offset Δ, calculated for various gain values (g=0.05 to 0.14 for plots from purple to green). Thick lines mark the stable self-localised solutions, both in the main graph and the inset, where it is reported the soliton frequency ϕ. Note that negative values of ϕ correspond to red-shifted frequencies with respect to the micro-cavity centre, in agreement with the experiments. The grey region marks the region of existence of the Lugiato-Lefever bright solitons. **b.** Intensity profile in the micro-cavity for a laser cavity-soliton (Δ =0.47; g= 0.14, blue line) and a Lugiato-Lefever cavity-soliton at the power threshold (orange line), highlighting the presence of a strong background in the Lugiato-Lefever case. **c.** Spectrum of the theoretical cases in b. The strong background of the Lugiato-Lefever cavity soliton results in a dominant comb mode at the centre of the spectrum. Laser cavity-soliton line generally possess higher power spectral density.

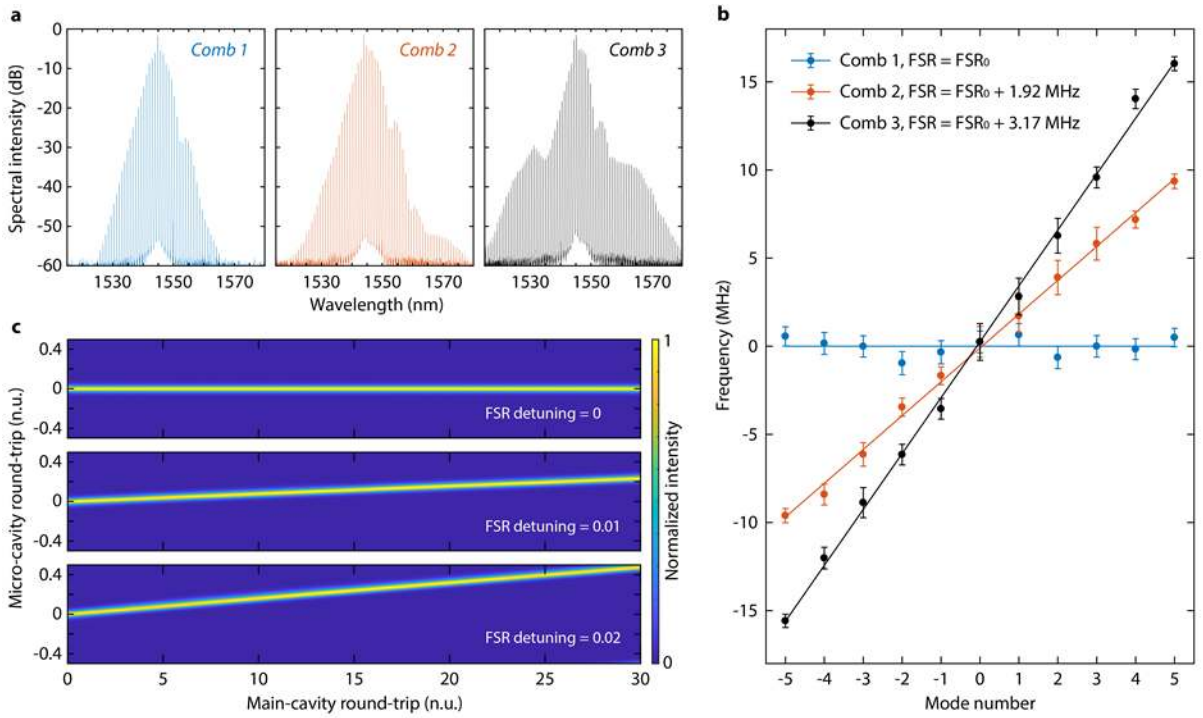

Figure 5. Temporal laser cavity-soliton repetition-rate control. a. Spectra. The fibre cavity length is changed within a broad range of 150 μm. Gain and losses had been readjusted to maintain the solitary state showing two equidistant solitons per round-trip; intra-cavity powers are 20 mW, 25 mW and 30 mW, in blue, orange and black, respectively. **b.** Residual frequency shift against mode number with respect to the best-fit for the Comb 1 case (blue). Combs 2 and 3 show a change in FSR and, hence, repetition-rate variations of 1.9MHz and 3.2MHz with respect to Comb 1. **c.** Calculated propagation of a stationary solitary solution when Δ =0.49 and g= 0.1, for $\delta = 0; 0.01; 0.02$. The solitary wave is maintained in all three cases.

Methods

Experimental Setup

The experimental setup is built around a high index doped silica integrated resonator with FSR~48.97 GHz and linewidth ΔF_A <140MHz (within the experimental measurement uncertainties), corresponding to a Q factor of ~1.3 million. The micro-resonator has a minimum in the transmission spectrum around 1552 nm, which is visible also in the comb generation and features transmission losses of 60%.

The micro-ring was inserted in an anomalous dispersion, polarisation-maintaining Ytterbium-Erbium co-doped fibre-cavity. This cavity comprised a delay line, polarisation optics, an optical isolator as well as a 10 nm tuneable bandpass filter (resulting, when matched to the amplifier spectral response, in a Gaussian linewidth of ΔF_F =650 GHz). Note that the soliton spectra in Fig. 3 and 4 well exceed such a bandwidth. The FSR of the cavity was about 77 MHz.

In sharp contrast to passively mode-locked lasers that intrinsically need a gain-dampening mechanism, cavity-solitons do not necessitate a fast-saturable absorption because they arise from the bistability of the system [22]. For this reason, we used a full polarisation-maintaining loop to prevent any effect related to fast gain saturation and standard passive mode-locking, further confirming the bistable origin of the pulses. Note that the fibre amplifier had a recovery time in the order of 10 ms [42], well above the soliton repetition-rate and main-cavity round-trip.

The intra-cavity lines were measured by laser-scanning spectroscopy (Supplementary). The scanning laser was calibrated with a 6.95 MHz Mach-Zehnder and by beating it with a 250MHz reference comb [43]. The micro-comb output was extracted at the drop-port of the micro-ring and was characterised with a second harmonic generation, background-free, non-collinear autocorrelator, optical spectrum-analyser and radio-frequency detection, obtained with a fast oscilloscope. The intra-cavity energy was measured with two monitors at the drop-port of the micro-resonator and the output of the amplifier before all system losses.

The soliton cases presented in the experiments show the presence of multiple pulses in the cavity. Our present setup could not run at a lower saturation powers which would allow for the observation of single soliton states.

Soliton states could be maintained over a time scale of minutes. The long-term stability of the solitary state was limited by mechanical and acoustical perturbations. Electronic feedback and proper packaging to screen mechanical and acoustical perturbations is expected to improve the system stability.

Model

The main features of the laser can be obtained by a simple mean-field model (see Supplementary for the complete derivation) that, in its normalised form, reads:

$$\partial_t a + \frac{i\zeta_a}{2}\partial_{xx} a + i\,|a|^2 a = -\kappa a + \sqrt{\kappa}\sum_{q=-N}^{N} b_q \quad (3)$$

$$\partial_t b_q + \delta\partial_\tau b_q + \frac{i\zeta_b}{2}\partial_{xx} b_q - 2\pi\, i\,(\Delta - q) b_q = \sigma\partial_{xx} b_q + g\, b_q - \sum_{p=-N}^{N} b_p + \sqrt{\kappa} a, \quad (4)$$

where a and b_q are the optical field envelopes for the micro-resonator and amplifying cavities, respectively, and are expressed as a function of the normalised propagation time t and space coordinate x. Here we have considered the generic interaction with 2N+1 super-modes b_q, for $|q| \leq N$; the mode with $q=0$ corresponds to the leading mode.

The time t accounts for the propagation over different round-trips and is normalised against the main-cavity round-trip $T_b=1/F_b$=12.5 ns. The space coordinate x, defined for $|x|<1/2$, is associated to the frame moving with the pulse and is normalised against the micro-cavity round-trip length, which corresponds to a round-trip time $T_a=1/F_a$ =20 ps.

The left- and right-hand sides of the equations contain the conservative and dissipative terms: $\zeta_{(a,b)}>0$, Δ and δ are the normalised coefficients for the cavity (anomalous) dispersions, the cavity-frequency offset and the group velocity mismatch. The latter term considers the effective FSR detuning between the two cavities as in Eq. (1); κ, g and σ represent the coupling, saturated gain and bandwidth of the spectral-filtering, respectively.

Specifically (see Supplementary for the derivation), the normalised coupling parameter is $\kappa = \pi \Delta F_A T_b \approx 2\pi$, being the micro-cavity linewidth ΔF_A approximately twice the FSR of the main-cavity (in the experimental condition). The normalised dispersions are $\zeta_{(a,b)} = -\beta_{(a,b)} v_{(a,b)} T_b / T_a^2$ for which $v_{(a,b)}$ and $\beta_{(a,b)}$ are the group-velocities and group velocity dispersions of the two cavities, respectively. In the simulations, we used $\zeta_a = 1.25 \times 10^{-4}$, $\zeta_b = 3.5 \times 10^{-4}$, obtained with values $|\beta_a|$≈-20 ps²/km and $|\beta_b|$≈-60 ps²/km (within our experimental constraints). We used a gain bandwidth $\sigma = (2\pi T_a \Delta F_F)^{-2} \approx 1.5 \times 10^{-4}$, based on a 650 GHz intra-cavity spectral filter. The gain g, considered as the saturated-gain of the amplifier, is normalised against the main-cavity length and, together with Δ and δ in Eq. (1), is an adjustable parameter in our numerical datasets.

The stationary states are defined as $a(t,x) = a_S(x - vt)\exp[2\pi i\phi t]$, $b_q(t,x) = b_{q,S}(x - vt)\exp[2\pi i\phi t]$, where the normalised frequency offset ϕ and the normalised velocity v are as in Eq. (2). Solitary solutions are found by numerical continuation considering 11 super-modes (i.e. with N=5), while stability is investigated with linear perturbation analysis and propagation considering 61 super-modes (i.e. with N=30).

Acknowledgment

We acknowledge the support of the U.K. Quantum Technology Hub for Sensors and Metrology, EPSRC, under Grant EP/M013294/1 and from INNOVATE UK, project 'IOTA' grant agreement EP/R043566/1. A.P. acknowledges the support from the People Programme (Marie Curie Actions) of the European Union's FP7 Programme under REA grant agreement CHRONOS (327627). M.P. acknowledges the support by EU-H2020, research and innovation programme under REA grant agreement TIMING (725046) and from the People Programme (Marie Curie Actions) of the European Union's FP7 Programme under REA grant agreement THEIA (630833). B.W. acknowledges the support from the People Programme (Marie Curie Actions) of the European Union's FP7 Programme under REA grant agreement INCIPIT (PIOF-GA-2013-625466).

R.M. acknowledges funding by the Natural Sciences and Engineering Research Council of Canada (NSERC) through the Strategic, Discovery, and Acceleration Grants Schemes, by the MESI PSR-SIIRI Initiative in Quebec, by the Canada Research Chair Program, as well as additional support by the Government of the Russian Federation through the ITMO Fellowship and Professorship Program (grant 074-U 01) and by the 1000 Talents Sichuan Program.

Author Contributions

A.P., H.B. and M.P. developed the original concept. B.E.L. and S.T.C. designed and fabricated the integrated devices. H.B performed the experiments. A.P developed the theoretical model. A.C., M.R., L.D.L., J.S.T.G., G.-L.O., D.J.M., R.M. and B.W. contributed to the development of the experiment, numerical model and to the data analysis. A.P., B.W., G.-L.O., D.J.M., R.M., H.B. and M.P. contributed to the writing of the manuscript. B.W., M.P., and A.P. supervised the research.

References

[1] Kippenberg, T. J., Holzwarth, R. & Diddams, S. A. Microresonator-based optical frequency combs. *Science* **332**, 555–559 (2011).

[2] Pasquazi, A. et al. Micro-combs: A novel generation of optical sources. *Phys. Rep.* **729**, 1-81 (2017).

[3] Suh, M.-G., Yang, Q.-F., Yang, K. Y., Yi, X. & Vahala, K. J. Microresonator soliton dual-comb spectroscopy. *Science* **354**, 600–603 (2016).

[4] Yu, M. et al. Silicon-chip-based mid-infrared dual-comb spectroscopy. *Nat. Commun.* **9**, 1869 (2018).

[5] Marin-Palomo, P. et al. Microresonator-based solitons for massively parallel coherent optical communications. *Nature* **546**, 274–279 (2017).

[6] Pfeifle, J. et al. Optimally Coherent Kerr Combs Generated with Crystalline Whispering Gallery Mode Resonators for Ultrahigh Capacity Fiber Communications. *Phys. Rev. Lett.* **114**, 093902 (2015).

[7] Liang, W., Eliyahu, D., Ilchenko, V. S., Savchenkov, A. A., Matsko, A. B., Seidel, D., & Maleki, L. High spectral purity Kerr frequency comb radio frequency photonic oscillator. *Nat. Commun.* **6**, 7957 (2015).

[8] Spencer, D. T. et al. An Optical-Frequency Synthesizer Using Integrated Photonics, *Nature* **557**, 81-85 (2018).

[9] Trocha, P. et al. Ultrafast optical ranging using microresonator soliton frequency combs. *Science* **359**, 887-891 (2018).

[10] Suh, M.-S. & Vahala, K. J. Soliton microcomb range measurement. *Science* **359**, 884-887 (2018).

[11] Kues, M. et al. On-chip generation of high-dimensional entangled quantum states and their coherent control. *Nature* **546**, 622–626 (2017).

[12] Reimer, C. et al. Generation of multiphoton entangled quantum states by means of integrated frequency combs. *Science* **351**, 1176-1180 (2016).

[13] Brasch, V. et al. Photonic chip–based optical frequency comb using soliton Cherenkov radiation. *Science* **351**, 357–360 (2016).

[14] Del'Haye, P. et al. Phase-coherent microwave-to-optical link with a self-referenced microcomb. *Nat. Photonics* **10**, 516-520 (2016).

[15] Suh, M.-G. et al. Searching for exoplanets using a microresonator astrocomb. *Nat. Photonics* 13, 25-30 (2019).

[16] Obrzud, E. et al. A microphotonic astrocomb. *Nat. Photonics* 13, 31-35 (2019).

[17] Haelterman, M., Trillo, S. & Wabnitz, S. Dissipative modulation instability in a nonlinear dispersive ring cavity. *Opt. Commun.* **91**, 401-407 (1992).

[18] Leo, F. et al. Temporal cavity-solitons in one-dimensional Kerr media as bits in an all-optical buffer. *Nat. Photonics* **4**, 471–476 (2010).

[19] Herr, T. et al. Temporal solitons in optical microresonators. *Nat. Photonics* 8, 145–152 (2013).

[20] Xue, X. et al. Mode-locked dark pulse Kerr combs in normal-dispersion microresonators. *Nat. Photonics* **9**, 594–600 (2015).

[21] Cole, D. C., Lamb, E. S., Del'Haye, P., Diddams, S. A. & Papp, S. B. Soliton crystals in Kerr resonators. *Nat. Photonics* **11**, 671–676 (2017).

[22] Lugiato, L. A., Prati, F. & Brambilla, M. Nonlinear Optical Systems. (Cambridge University Press, 2015).

[23] Xue, X., Wang, P.-H., Xuan, Y., Qi, M. & Weiner, A. M. Microresonator Kerr frequency combs with high conversion efficiency. *Laser Photonics Rev.* **11**, 1600276 (2017).

[24] Yao, B. et al. Gate-tunable frequency combs in graphene–nitride microresonators. *Nature* **558**, 410-414 (2018).

[25] Tanguy, Y., Ackemann, T., Firth, W. J. & Jäger, R. Realization of a Semiconductor-Based Cavity Soliton Laser. *Phys. Rev. Lett.* **100**, 013907 (2008).

[26] Barland, S. et al. Cavity-solitons as pixels in semiconductor microcavities. *Nature* **419**, 699–702 (2002).

[27] Genevet, P., Barland, S., Giudici, M. & Tredicce, J.R. Cavity Soliton Laser based on Mutually Coupled Semiconductor Microresonators. *Phys. Rev. Lett.* **101**, 123905 (2008).

[28] Marconi, M., Javaloyes, J., Balle, S. & Giudici, M. How Lasing Localized Structures Evolve out of Passive Mode Locking. *Phys. Rev. Lett.* **112**, 223901 (2014).

[29] Wright, L. G., Christodoulides, D. N. & Wise, F. W. Spatio-temporal mode-locking in multimode fiber lasers. *Science* **358**, 94–97 (2017).

[30] Grelu, P. & Akhmediev, N. Dissipative solitons for mode-locked lasers. *Nat. Photonics* **6**, 84–92 (2012).

[31] Stern B., Ji X., Okawachi Y., Gaeta A.L., Lipson M. Battery-operated integrated frequency comb generator. *Nature* **562**, (7727), 401 (2018).

[32] Obrzud, E., Lecomte, S. & Herr, T. Temporal solitons in microresonators driven by optical pulses. *Nat. Photonics* **11**, 600–607 (2017).

[33] Yang, Q.-F., Yi, X., Yang, K. Y. & Vahala, K. Counter-propagating solitons in microresonators. *Nat. Photonics* **11**, 560–564 (2017).

[34] Miller, S. A. et al. Tunable frequency combs based on dual microring resonators, *Opt. Express* **23**, 21527–21540 (2015).

[35] Gustave, F. et al. Observation of Mode-Locked Spatial Laser Solitons. *Phys. Rev. Lett.* **118**, 044102 (2017).

[36] Krupa, K. et al. Spatial beam self-cleaning in multimode fibres. *Nat. Photonics* **11**, 237–241 (2017).

[37] Scroggie, A.J., Firth, W.J. & Oppo, G.-L. Cavity-soliton laser with frequency selective feedback, *Phys. Rev. A* **80**, 013829 (2009).

[38] Peccianti, M. et al. Demonstration of a stable ultrafast laser based on a nonlinear microcavity. *Nat. Commun.* **3**, 765 (2012).

[39] Wang, W. et al. Repetition rate Multiplication Pulsed Laser Source Based on a Microring Resonator. *ACS Photon.* **4**, 1677–1683 (2017).

[40] Bao H., Cooper A., Chu S.T., Moss D.J., Morandotti R., Little B.E., Peccianti M., Pasquazi A. Type-II Micro-comb generation in a filter-driven four wave mixing laser. *Photonics Research Journal* **6**, (5) B67-B73 (2018).

[41] Andral, U., Si Fodil, R., Amrani, F., Billard, F., Hertz, E. & Grelu, Ph. Fiber laser mode locked through an evolutionary algorithm. *Optica* **2**, 275-278 (2015).

[42] Haboucha, A., Leblond, H., Salhi, M., Komarov, A. & Sanchez, F. Analysis of soliton pattern formation in passively mode-locked fiber lasers. *Phys. Rev. A* **78**, 043806 (2008).

[43] Del'Haye, P., Arcizet, O., Gorodetsky, M. L., Holzwarth, R. & Kippenberg, T. J. Frequency comb assisted diode laser spectroscopy for measurement of microcavity dispersion. *Nat. Photonics* **3**, 529–533 (2009).

Laser Cavity-Soliton Micro-Combs
Supplementary Materials

Hualong Bao[1], Andrew Cooper[1], Maxwell Rowley[1], Luigi Di Lauro[1], Juan Sebastian Totero Gongora[1], Sai T. Chu[2], Brent E. Little[3], Gian-Luca Oppo[4], Roberto Morandotti[5,6,7], David J. Moss[8], Benjamin Wetzel[1], Marco Peccianti[1] and Alessia Pasquazi[1*]

[1] *Emergent Photonics (Epic) Lab, Dept. of Physics and Astronomy, University of Sussex, BN1 9QH, UK*
[2] *Department of Physics, City University of Hong Kong, Tat Chee Avenue, Hong Kong, China SAR*
[3] *State Key Laboratory of Transient Optics and Photonics, Xi'an Institute of Optics and Precision Mechanics, CAS, Xi'an, China*
[4] *SUPA, Department of Physics, University of Strathclyde, Glasgow, United Kingdom*
[5] *INRS-EMT, 1650 Boulevard Lionel-Boulet, Varennes, Québec, Canada J3X 1S2*
[6] *Institute of Fundamental and Frontier Sciences, University of Electronic Science and Technology of China, Chengdu 610054, Sichuan, China*
[7] *ITMO University, St. Petersburg 199034, Russia*
[8] *Centre for Microphotonics, Swinburne University of Technology, Hawthorn, VIC 3122, Australia*

** Corresponding author: a.pasquazi@sussex.ac.uk*

Section SM1: Derivation of the Model Equations

Our experimental configuration can be described by a system comprising two travelling-wave resonators, as depicted in Fig. S1a. Such a system features a Kerr cavity ('a', red circle) nested in an amplifying main-cavity ('b', black loop). In our experiments, such cavities are, respectively, a micro-ring resonator and a fibre-loop with gain. The amplifying-cavity is effectively an open loop, linked to the input and output ports of the ring. For simplicity, we model it as a closed cavity, adding an effective length of approximately half the circumference of the ring between these two connection points. The main-cavity field at the input of the amplifying loop is subtracted and replaced by the evolution of the input field after propagating in the ring (typically, half circumference).

In a more formal description, we define two space coordinates $X_{(a,b)}$ for the two cavities, with coupling points at $X_{(a,b)} = 0$ and $X_{(a,b)} = L_{(a,b)}^{(1)}$. The minimum propagation path of a pulse within the micro-cavity is $L_a = L_a^{(1)} + L_a^{(2)}$, which corresponds to a round-trip time T_a. Because there is no physical connection between points $X_b = L_b^{(1)}$ and $X_b = 0$ of the gain loop, a pulse propagating in the main-cavity necessarily travels the micro-cavity section $L_a^{(2)}$ so that the minimum propagation path is, in this case, $L_b^{(1)} + L_a^{(2)}$.

Therefore, in our model it is convenient to consider the main-cavity as closed with an adjusted round-trip time T_b, obtained by adding an auxiliary length $L_b^{(2)} \approx L_a^{(2)}$ between the points $X_b = L_b^{(1)}$ and $X_b = 0$ (Fig. S1a, dashed black line) so that the total length of the cavity is, consequently, $L_b = L_b^{(1)} + L_b^{(2)}$. The length $L_b^{(2)}$ will be exactly defined below and we will properly configure the

optical field at the main-cavity input point $X_b = 0$, so that it will depend only on the field in the micro-resonator at the point $X_a = L_a$.

We consider $T_b \gg T_a$ and define an integer M which approximately represents the ratio between the two round-trips. Such a quantity allows us to count how many modes of the long cavity are contained in the free-spectral range (FSR) of the micro-cavity, Fig. S1b. Specifically, we have

$$F_a = (M - \delta)F_b, \tag{S1}$$

with the FSR given by $F_{(a,b)} = T_{(a,b)}^{-1}$ for the two cases. The variable $|\delta| < 1/2$ represents the FSR detuning, as in Eq. (1) in the main text, and allows for modelling non-commensurate loops, i.e. for periods T_b which are not exactly divided by T_a.

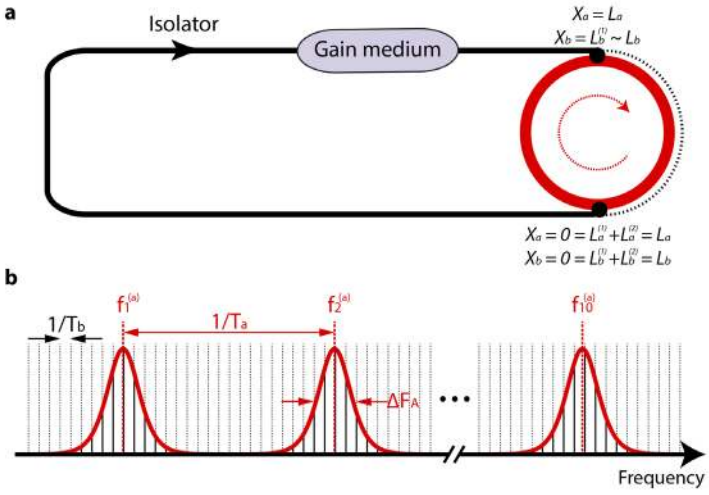

Figure S1. Principle of operation. a. *Scheme of the nested, travelling-wave cavities configuration: a Kerr micro-cavity ('a' – red loop, with length $L_a = L_a^{(1)} + L_a^{(2)}$), is nested in an amplifying main cavity ('b' – black line, with length $L_b = L_b^{(1)} + L_b^{(2)}$). We define two space coordinates $X_{(a,b)}$ for the two cavities, with coupling points at $X_{(a,b)} = 0$ and $X_{(a,b)} = L_{(a,b)}^{(1)}$.* ***b.*** *Scheme of the modes interaction, with the resonances of the micro-cavity (red) and modes of the main-cavity (black). The Kerr micro-cavity resonances possess a linewidth ΔF_A and each mode (of index m) a central frequency $f_m^{(a)}$.*

The optical fields in the two cavities $A(T, X_a)$ and $B(T, X_b)$ are expressed in $[\sqrt{\mathrm{W}}]$ and are slowly varying in time T, defined in [s].

It is convenient to expand such functions in a set of cavity modes $a_m(T)$ and $b_n(T)$, defined in $[\sqrt{\mathrm{J}}]$ (as usually done in coupled-mode theory) [1] and given by

$$A(T, X_a) = \sum_{m=-\infty}^{\infty} \frac{a_m(T)}{\sqrt{T_a}} \exp\left[2\pi i m \frac{X_a}{L_a}\right], \tag{S2}$$

$$B(T, X_b) = \sum_{n=-\infty}^{\infty} \frac{b_n(T)}{\sqrt{T_b}} \exp\left[2\pi i n \frac{X_b}{L_b}\right]. \tag{S3}$$

In this way, we can study their dynamics using a set of very general, standard coupled-mode equations [1] for all the interacting modes, which can be generalised for a large class of resonator types. Specifically, our full model, which accounts for the whole dynamic, reads as

$$\frac{da_m}{dT} = -\left[2\pi\, i\, f_m^{(a)} + \pi\, \Delta F_A + i\frac{v_a\beta_a}{2}(2\,\pi f_m^{(a)})^2\right] a_m - \frac{i\gamma v_a}{T_a}\sum_{j,p,l}\delta_{j-m,p-l}\, a_j a_l a_p^* + \frac{S_a}{\sqrt{T_a}}, \quad \text{(S4)}$$

$$\frac{db_n}{dT} = -\left[2\pi\, i\, f_n^{(b)} - G\, v_b + \left(i\frac{v_b\beta_b}{2} + \frac{1}{(2\pi\,\Delta F_F)^2 T_b}\right)(2\,\pi\, f_n^{(b)})^2\right] b_n + \frac{S_b}{\sqrt{T_b}}, \quad \text{(S5)}$$

where $v_{(a,b)}$ and $\beta_{(a,b)}$ are the group-velocities and group velocity dispersions of the two cavities, respectively and $\delta_{i,j}$ is the Kronecker delta. Every $a_m$or b_n mode oscillates at the frequencies

$$f_m^{(a)} = m\, F_a, \quad \text{(S6)}$$

$$f_n^{(b)} = (n - \Delta) F_b, \quad \text{(S7)}$$

respectively. With this definition, we fix the central mode of the micro-cavity a_0 to a frequency $f_0^{(a)} = 0$, while the frequency $f_0^{(b)} = -F_b\,\Delta$ of the central laser cavity mode $b_0(t)$ is detuned via the parameter Δ, which is the normalised frequency offset with respect to the central micro-cavity frequency $f_0^{(a)} = 0$. Such offset is considered as a small value, in agreement with Eq. (1) in the main text.

We consider the waveguide dispersions $\beta_{(a,b)}$, in [s^2m^{-1}], the gain of the amplifying loop G, in [m^{-1}], the bandwidth ΔF_F of a band-pass filter in [Hz] and the Kerr waveguide coefficient γ, in $W^{-1}m^{-1}$ [2]. The parameter ΔF_A ,in [Hz], is the -3 dB linewidth of the micro-cavity resonance [1].

We can now discuss the source terms S_a and S_b, here expressed in [$\sqrt{W}$]. The cavities are coupled by means of the dimensionless coefficient $\sqrt{\theta}$ that we consider to be the same for the two ports, where θ is the ratio between the input and transmitted power in the coupler. Because the coupling losses are dominant in the micro-resonator, such a coefficient is related to the micro-cavity linewidth by $\theta = \pi\,\Delta F_A T_a$ [1].

The field coupled in the micro Kerr cavity, which is added to its intra-cavity field at the point $X_a = 0$, is the output field of the main-cavity in $X_b = L_b^{(1)}$, resulting in [1]:

$$\begin{aligned} S_a = \sqrt{\theta} B\left(T, L_b^{(1)}\right) &= \sqrt{\theta}\sum_{n=-\infty}^{\infty}\frac{b_n(T)}{\sqrt{T_b}}\exp\left[2\pi i n\frac{L_b - L_b^{(2)}}{L_b}\right] \\ &= \sqrt{\theta}\sum_{n=-\infty}^{\infty}\frac{b_n(T)}{\sqrt{T_b}}\exp\left[-2\pi i n\frac{L_a^{(1)}}{M L_a}\right], \end{aligned} \quad \text{(S8)}$$

where we have set $L_b^{(2)}/L_b = L_a^{(1)}/(M\,L_a)$. Such an equation will simplify the calculation later.

The definition of the source term S_b for the main-cavity needs to take into account that the main amplifying cavity is modelled as an effective open loop because in our experimental model there is no physical connection between the points $X_b = L_b^{(1)}$ and $X_b = L_b$ (black dashed line in Fig. S1a), as discussed at the beginning of this section. Such a modelling can be done imposing that the input field in the amplifying loop at $X_b = 0$ is only dependent on the micro-cavity coupled field, i.e. $B(T,0) = \sqrt{\theta}A(T, L_a^{(1)})$. From a practical point of view, this requires subtracting the field $B(T, L_b)$ propagating in the main-cavity just before the coupling point $X_b = 0$ in the source term,

$$S_b = \sqrt{\theta} A\left(T, L_a^{(1)}\right) - B(T, L_b) = \sum_{m=-\infty}^{\infty} \sqrt{\theta} \frac{a_m(T)}{\sqrt{T_a}} \exp\left[2\pi i m \frac{L_a^{(1)}}{L_a}\right] - \frac{b_m(T)}{\sqrt{T_b}}. \quad \text{(S9)}$$

Eqs. (S1)-(S9) define the full model which can be used to simulate the complete dynamic of the system and it is equivalent to the model described in Ref. [3]. Mean-field models, however, usually allow for better understanding of the physical dynamics and, for this reason, we will reduce Eqs. (S1)-(S9) with standard phase-matching considerations [2] to a set of partial differential equations.

In principle, Eqs. (S8) and (S9) couple all the b_n modes, both together and to every a_m mode. Practically, however, only modes with similar frequencies will interact [1]: the strongest interaction with the Kerr cavity frequency $f_m^{(a)}$ will occur for the main-cavity frequencies $f_n^{(b)}$ falling within the micro-cavity linewidth ΔF_A:

$$\left|f_n^{(b)} - f_m^{(a)}\right| < \Delta F_A. \quad \text{(S10)}$$

It is therefore important to express the main-cavity frequencies $f_n^{(b)}$ in terms of the Kerr cavity frequencies $f_m^{(a)}$ to allow a better comparison between the interacting frequencies. Considering that every FSR of the micro-cavity contains almost M $f_n^{(b)}$ frequencies (see Eq. (S1) and Fig. S1b), we express the index n of the b_n set as

$$n = m\,M + q, \quad \text{(S11)}$$

where m spans all the integer spectrum while $|q| < M$. Using the definition of the integer M given in Eq. (S1), we get

$$f_n^{(b)} = (m\,M + q - \Delta)F_b = m\,F_a + (q - \Delta + m\,\delta)F_b = f_m^{(a)} - (\Delta - q - m\,\delta)F_b. \quad \text{(S12)}$$

The index m can now be used to refer the main-cavity mode directly to the frequency $f_m^{(a)}$ of the micro-cavity. The parameter q is, conversely, a relative index referring to the frequency of the a_m mode. Following our discussion in the main text, it defines the order of the *super-mode*: in particular, $q = 0$ is associated to the leading-order mode. In general, q selects a set of main-cavity, equally-spaced modes . When the FSR of the two cavities is commensurate, i.e. $\delta = 0$, such modes are exactly set apart by the micro-cavity FSR F_a. The super-modes and, practically, the index q are very useful to select the interacting frequencies, although the number of modes necessary for correctly describing the interaction is difficult to determine *a priori*. We can, however, define an integer N and keep only the super-modes with $|q| < N$. We expect that the number $2N + 1$ of main-cavity modes per micro-cavity resonance will be around the order of magnitude of the main-cavity mode number per micro-cavity lines $\Delta F_A/F_b$ and, in any case, much smaller than the ratio M between the two cavities' FSRs (Eq. (S1)). The validity of the solution can be simply checked *a posteriori* by testing the model for increasing N, as we will do in the following.

We can now look into a field expression for a single super-mode and, to this aim, we group together all the modes $b_n = b_{mM+q}$ with the same q and Fourier transform them in the space X_a of the micro-cavity

$$B_q(T, X_a) = \sum_{m=-\infty}^{\infty} \frac{b_{m\,M+q}\,(T)}{\sqrt{T_b}} \exp\left[2\pi i m\,\frac{\left(X_a - L_a^{(1)}\right)}{L_a}\right]. \tag{S13}$$

Without loss of generality, we have centred the mode in $L_a^{(1)}$ because it is convenient in the following substitutions.

Now that both the micro- and main-cavity fields are defined in the same space, we derive a mean-field system via multiplying Eqs. (S4) and (S5) by the terms $\exp[2\pi i m\, X_a L_a^{-1}]$ and $\exp\left[2\pi i m\,\left(X_a - L_a^{(1)}\right) L_a^{-1}\right]$, respectively. We will then keep only a small number $2N + 1 << M$ of main-cavity modes per micro-cavity resonance: the mode $b_{m\,M+q}$ will interact with the mode a_m only if $|q| < N$. Summing up for every m and, by using Eqs. (S2) and (S13), we get

$$T_a \frac{\partial A}{\partial T} + L_a \frac{\partial A}{\partial X_a} - L_a \frac{i\beta_a v_a^2}{2} \frac{\partial^2 A}{\partial X_a^2} + i\gamma\, L_a |A|^2 A = -\theta A + \sqrt{\theta} \sum_{q=-N}^{N} B_q, \tag{S14}$$

$$\begin{aligned} T_b \frac{\partial B_q}{\partial T} + M\, L_a \frac{\partial B_q}{\partial X_a} - L_b \frac{i\beta_b v_a^2}{2} \frac{\partial^2 B_q}{\partial X_a^2} - 2\pi i(\Delta - \mathrm{q}\,) B_q \\ = \frac{v_a^2}{(2\pi\,\Delta F_F)^2} \frac{\partial^2 B_q}{\partial X_a^2} + G L_b\, B_q - \sum_{p=-N}^{N} B_p + \sqrt{\theta} A, \end{aligned} \tag{S15}$$

where we have neglected the contribution of the small detuning $q + \Delta + m\,\delta$ in the dispersion and of the small-phase terms q/M. The equations reported in the main text are found with the following normalisation. The propagating time is normalised against the main-cavity period in the frame moving with the pulses, $t = T\,T_b^{-1}$, while the fast cavity-time, $x = X_a L_a^{-1} - T\,T_a^{-1}$, is normalised against the micro-cavity roundtrip. We have $a = A\sqrt{\gamma v_a T_b}$, $b_q = B_q\,T_b\sqrt{\gamma v_a\,T_a^{-1}}$, $g = G\,L_b$, $\zeta_{(a,b)} = -\beta_{(a,b)} v_{(a,b)} T_b T_a^{-2}$, $\sigma = (2\pi\,\Delta F_F T_a)^{-2}$. Note that the coupling parameter $\kappa = \theta T_b F_a = \pi\,\Delta F_A\,T_b$ provides directly the number $\kappa\pi^{-1}$ of main-cavity modes per micro-ring resonance. Tables 1 and 2 in the Appendix summarise all the quantities used in the simulations.

Finally, we note that such a reduction could be also performed starting from a set of propagation equations, as modelled in Ref. [3], by applying a similar method to Ref. [4].

Section SM2: Soliton Search and Analysis

We start from the general system used in the main text involving the coupled interaction of 2N+1 super-modes

$$\partial_t a + \frac{i\zeta_a}{2} \partial_{xx} a + i\,|a|^2 a = -\kappa a + \sqrt{\kappa} \sum_{q=-N}^{N} b_q, \tag{S16}$$

$$\partial_t b_q + \delta \partial_x b_q + \frac{i\zeta_b}{2} \partial_{xx} b_q - 2\pi\, i\,(\Delta - q) b_q = \sigma \partial_{xx} b_q + g\, b_q - \sum_{p=-N}^{N} b_p + \sqrt{\kappa} a. \tag{S17}$$

The aim of this section is to find localised solutions of the kind $a(t, x) = a_S(x - vt)\exp[2\pi i\phi t]$, $b_q(t, x) = b_{q,S}(x - vt)\exp[2\pi i\phi t]$, where the variable ϕ is the normalised frequency of the pulse and v the normalised velocity, as defined in the main text. We will do such a search via numerical

integration. Before starting with the integration, it is convenient to do some analytical considerations that will help us in defining the range of parameters where stable solitons exist. For this reason, we focus first on the case $N = 0$, involving only the mode $b_0(t, x)$: the study of the soliton behaviours in such a system is then associated directly with the leading cavity super-mode (experiencing the lowest coupling losses) responsible for driving the predominant dynamics and, thus, providing a general understanding of the full system. Eqs (S16) and (S17) simplify in a two-equations system

$$\partial_t a + \frac{i\zeta_a}{2}\partial_{xx} a + i\,|a|^2 a = -\kappa a + \sqrt{\kappa} b_0, \tag{S18}$$

$$\partial_t b_0 + \delta\partial_x b_0 + \frac{i\zeta_b}{2}\partial_{xx} b_0 - 2\,\pi i\Delta\, b_0 = \sigma\partial_{xx} b_0 + (g-1)\, b_0 + \sqrt{\kappa} a, \tag{S19}$$

where we will assume $\zeta_a > 0$ to study bright localised states [5]. The system possesses strong similarities with the model for semiconductor solitons in frequency-selective feedback cavities and with dual-core fibre laser systems [6, 7], although it has the fundamental peculiarity of showing nonlinearity and gain in two different equations which, different from previous studies, allows the formation of broadband solutions in the Kerr cavity.

The existence of cavity-solitons generally requires bistability, i.e. the contemporary presence of two stationary states, a high-energy and a low-energy state (or background) upon which the soliton is formed. In the field of micro-combs, this has been largely discussed for Lugiato-Lefever temporal cavity solitons usually forming over a continuous-wave (CW) background; the Lugiato-Lefever equation, with the conventions used in this paper, reads as

$$\partial_t a + \frac{i\zeta_a}{2}\partial_{xx} a + i\,|a|^2 a - 2\,\pi i\Delta\, a = -\kappa a + \sqrt{\kappa}\, S, \tag{S20}$$

for the same dispersion ζ_a, coupling constant κ and field a of the micro-cavity in (S18) and with S as the external driving field, detuned from the coupled resonance by the frequency offset Δ. The threshold for bistability of Eq. (S20) requires $\Delta < \kappa\sqrt{3}$ and $|S|^2 > 8/(3\sqrt{3})\,\kappa^2$ [8], which provides a minimum threshold excitation for soliton formation.

Conversely, in the system given by Eqs. (S18)-(S19), the two bistable stationary states are a CW state and a zero background. This is typical of homogeneous systems with gain, like in Refs. [6,7], where the null solution is admitted and usually exists in the full range of parameters, different from inhomogeneous, externally-driven systems, like in Eq. (S20). Eqs. (S18) and (S19) admit the two CW solution $|a_S|^2 = \pm\sqrt{g\,(1-g)^{-1}}\,(1-g+\kappa)$ with $\phi = -\Delta \pm (2\pi)^{-1}\sqrt{g(1-g)}$: their existence implies $0 < g < 1$. It is very important to stress that, different from Eq. (S20), the threshold for bistability is simply $g = 0$: any excitation above the zero level can, in principle, provide a localised state. The frequency offset should however be properly set as $\Delta_{\min} > -(2\pi)^{-1}\sqrt{g\,(1-g)^{-1}}|1-g+\kappa|$, which provides the existence of at least one CW state for Eqs (S18)-(S19).

The stability of the solitary states requires the stability of the low-energy stationary state, which here is the null solution. Note, however, that solitons are not the only stable solutions of a bistable system. Stable rolls and patterns, which originate from the modulation instability of the background, can be found in the instability region of the background itself. This is well-known for the Lugiato-Lefever system. The systematic study of these solutions is beyond the scope of this

paper, although such states are expected to exist also for our system in the region where the null background is unstable.

It is then very important to study the stability region of the zero state. Such a state is always unstable for frequency offsets $|\Delta| < (2\pi)^{-1}\sqrt{g\,(1-g)^{-1}}|1-g+\kappa|$. Although this formula is, in principle, valid only for Eqs. (S18)-(S19), the instability regions of Eqs. (S16)-(S17) are well approximated by $|\Delta+q| < (2\pi)^{-1}\sqrt{g\,(1-g)^{-1}}|1-g+\kappa|$ for $N > 0$. Figure S2 summarises the stability region of the zero state.

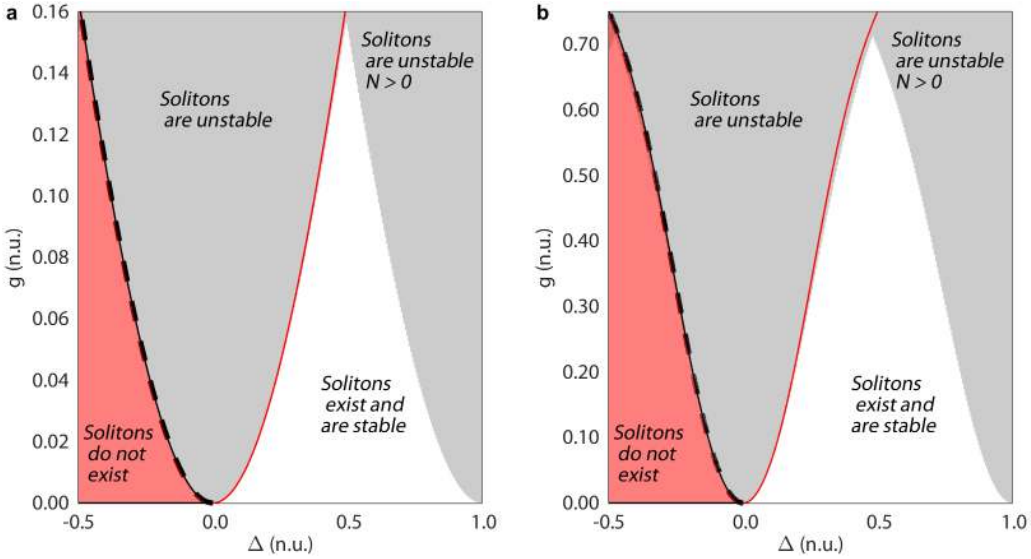

Figure S2. Region of existence and stability of solitary waves. *These existence maps refer to the solutions of Eq. (S18)-(S19). The stability map of these solutions, however, are discussed for the whole system, Eq. (S16)-(S17).* ***a.*** *Map for $\kappa = 2\pi$, as in the experiments. Solitons of Eq. (S18)-(S19) can be found for values larger than $\Delta_{min} > -(2\pi)^{-1}\sqrt{g\,(1-g)^{-1}}|1-g+\kappa|$, (black dashed line), where at least one CW state exists. The existence map, for simplicity, refers to Eq. (S18)-(S19). This threshold defines the region of existence of the soliton (non-existent in the light red region). The zero state of Eq. (S18)-(S19) is unstable for $|\Delta| < (2\pi)^{-1}\sqrt{g\,(1-g)^{-1}}|1-g+\kappa|$, (red solid line); note thst here solitons are also unstable. The general stability of the system needs to be evaluated on the system with N > 0. The stability of the zero solution for the case N = 5 is reported in the dark grey section. Stable solitons can be found in the white region.* ***b.*** *Map for $\kappa = \pi$. A smaller κ, which can be obtained with a shorter fibre cavity or a narrower micro-cavity linewidth, provides a larger stability region.*

These preliminary considerations help to restrict the range of parameters where interesting solitary solutions are expected. We now look numerically for localised states using the general system described by Eqs. (S16)-(S17). Starting from an appropriate guess solution, we use a numerical method (arc-length continuation [9]) for finding the soliton families of Eqs. (S16) and (S17). As discussed in the main text and reported in the Appendix, we use the parameters $\zeta_a = 1.25 \times 10^{-4}$, $\zeta_b = 3.5 \times 10^{-4}$, $\sigma = 1.5 \times 10^{-4}$ and $\kappa = 2\pi$, consistent with our experimental system.

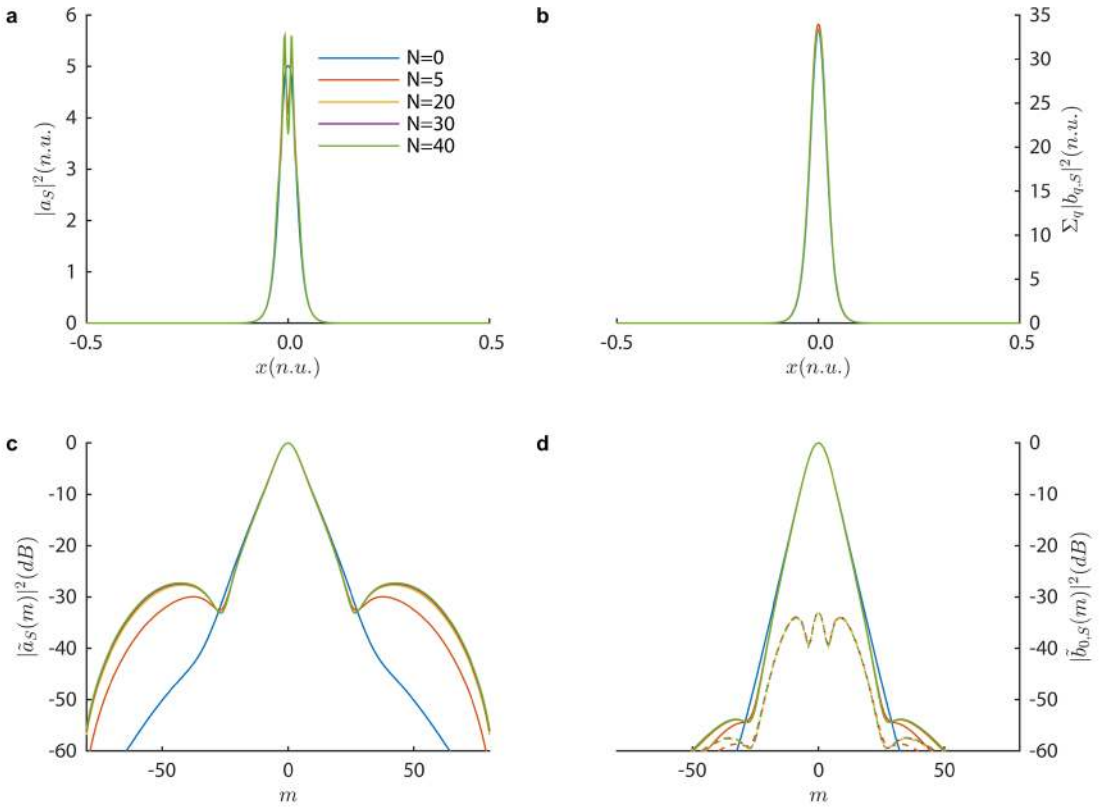

Figure S3. Solitary profile for different approximations of the number of super-modes N. *Here the cases for N = 0 (blue), N = 5 (orange), N = 20 (yellow), N = 30 (purple) and N = 40 (green) are reported.* ***a.*** *Time profiles of the field in the micro-cavity.* ***b.*** *Time profiles of the field in the main-cavity.* ***c.*** *Spectral intensity of the field in the micro-cavity.* ***d.*** *Spectral intensity of the field in the main-cavity. The spectral distribution of the first-order super-mode (q = 1) for the different cases is plotted with dashed lines in d. Here we have* $\zeta_a = 1.25 \times 10^{-4}$, $\zeta_b = 3.5 \times 10^{-4}$, $\sigma = 1.5 \times 10^{-4}$, $\kappa = 2\pi$, $g = 0.14, \delta = 0$ *and* $\Delta = 0.4763$*. It results in the following values:* $\phi = -0.4735$ *and* $v = 0$.

Figure S3 reports a comparison of the solitary profiles obtained with $N = 0$, $N = 5$, $N = 20$, $N = 30$ and N = 40 for $g = 0.14, \delta = 0$ and $\Delta = 0.4763$. This first test aims to set the number of modes N necessary for the numerical analysis. The difference from the case $N = 0$ is mostly visible in the spectral intensity plot[1] of the field, showing that the dominant dynamic is related to the leading modes. The cases $N = 20$, $N = 30$ and $N = 40$ are indiscernible over the entire spectral range. The case $N = 5$ provides a good approximation in this range of parameters. Higher-order modes in the micro-resonator (Fig. S2d), which are all locked to the soliton frequency $\phi = -0.4735$, here only appear -30 dB below the leading order: this analysis shows, however, that they contribute to provide a better spectral description of the comb.

[1] Fourier transform of the solution is defined as $\tilde{a}_S(m) = \int a_s(x) e^{-2i\pi m x} dx$ where m is the mode number.

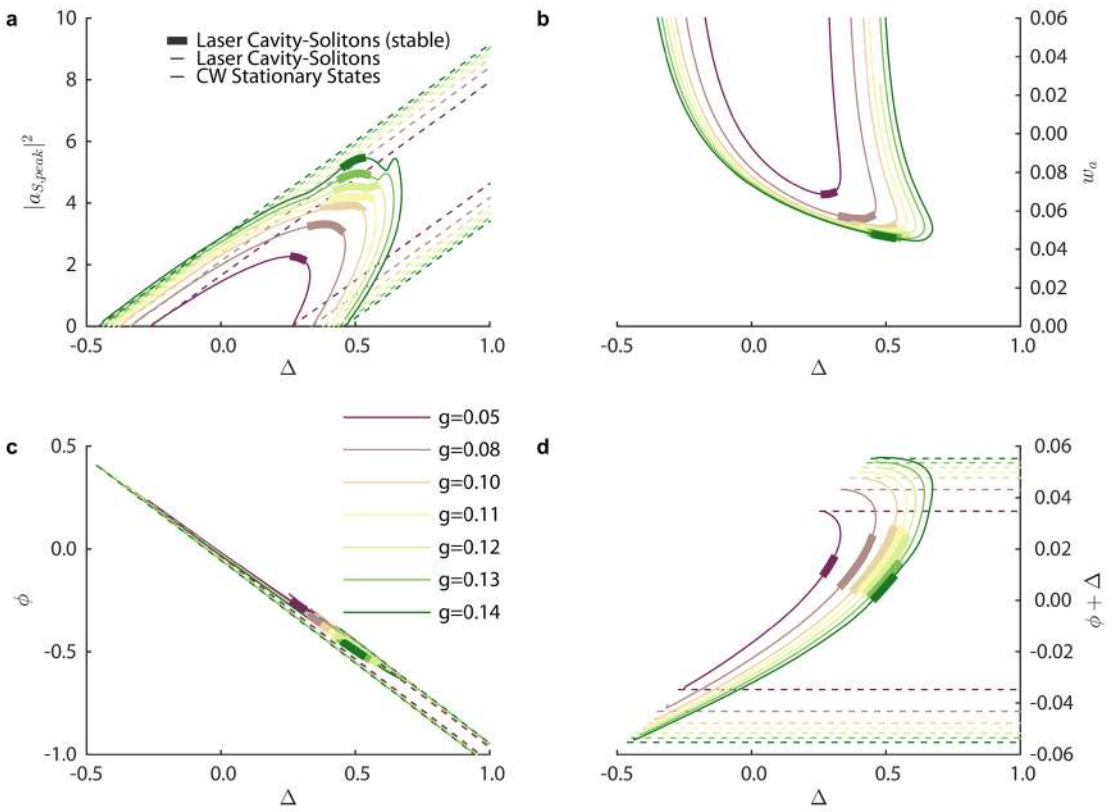

Figure S4. Map of Soliton States. *Stationary solutions for* $\zeta_a = 1.25 \times 10^{-4}$, $\zeta_b = 3.5 \times 10^{-4}$, $\sigma = 1.5 \times 10^{-4}$, $\kappa = 2\pi$, $\delta = 0$ *for* $g = 0.05, 0.08, 0.10, 0.11, 0.12, 0.13, 0.14$ *(plot colour scale ranging from purple to green, respectively). Thick lines mark stable solutions. a. Peak intensity of the solitary field in the micro-cavity vs frequency cavity offset* Δ *(full lines) with the corresponding two CW solutions (dashed lines) for* $\delta = 0$*. b. Pulse width of the micro-cavity intensity profile, defined as its standard deviation. c. Frequency of the soliton and of the CW solutions (solid and dashed lines respectively). d. Residual frequency* $\phi + \Delta$*.*

A general understanding of the behaviour for such solitary solutions can be obtained by analysing the fundamental soliton family as a function of the normalised frequency offset Δ, FSR detuning δ and gain g. First, we find the families by continuation for N = 5 and use standard linear perturbation analysis for defining their range of stability. Then, the stable solutions are propagated in a system with N = 30 to test their stability with a more accurate approximation.

The results obtained for $\delta = 0$ by varying Δ are reported in Fig. S4a for g ranging from 0.5 to 1.4. The peak intensity of $a_S(x)$ (i.e. for the micro-cavity field) is reported in Fig. S4a (full lines from purple to green), along with the peak intensity of the CW solutions, dashed lines. Stable solutions are marked with a thick line. Figure S4b depicts the solution pulse width w_a defined as the standard deviation of the intensity. Note also that the pulse gets narrower for increasing gain g, i.e. the spectrum broadens. Stable solutions correspond to the narrowest pulses. The frequency ϕ for the soliton (solid lines) along with the one for the CW stationary states (dashed lines) are reported in Fig. S4c. The frequency is better visualised by $\phi + \Delta$ in Fig. S4d, which shows that the oscillating frequency ϕ of the localised states is distinct from the CW case. It is very important to notice that stable states are obtained only for negative values of the oscillating frequency ϕ, which

means that the oscillating frequencies of a soliton state within the micro-cavity lines are red-detuned.

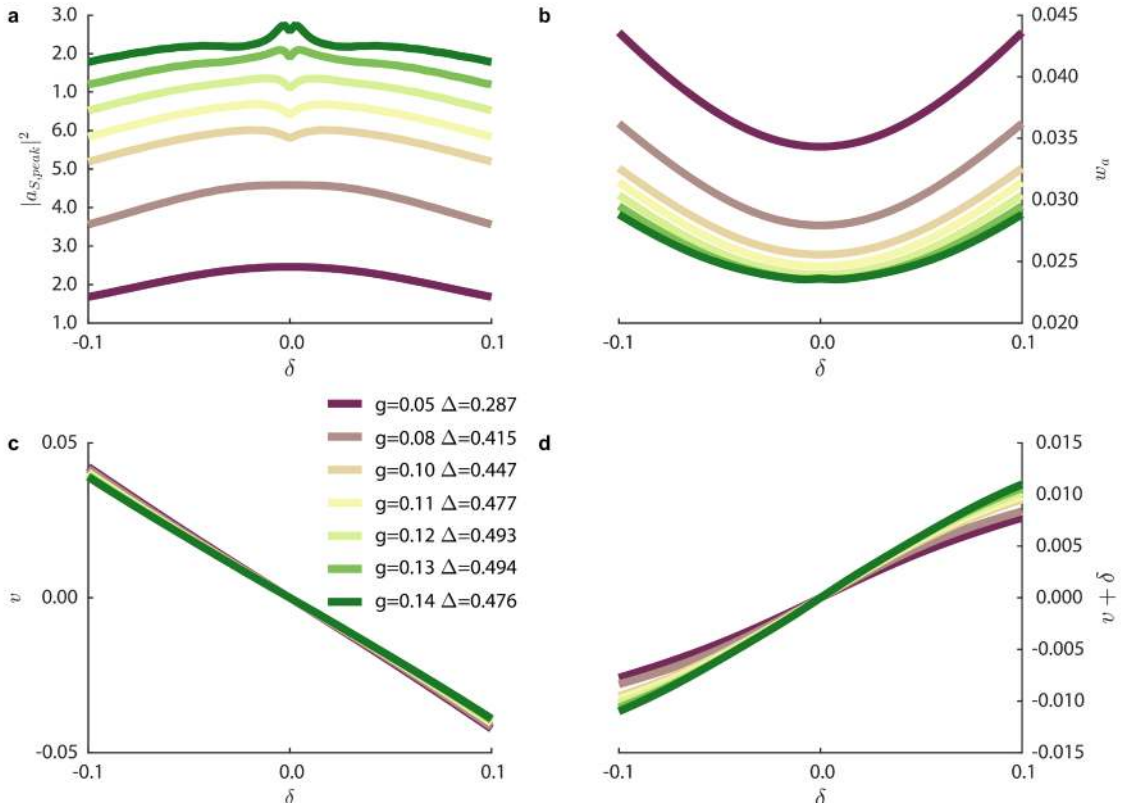

Figure S5. Map of Walking Soliton States. *Walking stationary solutions for* $\zeta_a = 1.25 \times 10^{-4}$, $\zeta_b = 3.5 \times 10^{-4}$, $\sigma = 1.5 \times 10^{-4}$, $\kappa = 2\pi$, *for* $g = 0.05, 0.08, 0.10, 0.11, 0.12, 0.13, 0.14$ *(plot colour scale ranging from purple to green). Here Δ= 0.2867, 0.4145, 0.4472, 0.4774, 0.4934, 0.4939, 0.4763.* ***a.*** *Peak intensity of the solitary field in the micro-cavity vs velocity mismatch* δ. ***b.*** *Pulse width.* ***c.*** *Velocity.* ***d.*** *Residual velocity* $v + \delta$.

After the analysis for stationary solitons, we look for so-called *walking* solitary solutions [8] (with a velocity v that is not zero) versus δ for the same range of gain used in the previous case. The offset Δ is chosen at the lowest border of the stability region. The peak intensity, pulse width and velocity of the micro-cavity field $a_S(x)$ are reported in Fig. S5. Remarkably, the state remains stable in the explored range.

Section SM3: Experimental Setup and Further Measurement Analysis

SM3.1: Experimental setup and intracavity laser-scanning spectroscopy.

Figure S6 reports the experimental setup. To characterise the micro-comb, we use its optical spectrum, the temporal autocorrelation obtained with a second harmonic non-collinear autocorrelator and the radio-frequency spectrum of the intensity, that allow us to evaluate the quality of the laser amplitude. In the results presented in Figs. 2 and 3 in the main text, the comb frequency lines have been also finely characterised by intra-cavity laser-scanning spectroscopy [10] (Fig. S5), which also revealed the position of the comb lines with respect to the micro-cavity resonances.

This is a very powerful approach which allowed us to experimentally extract the variables ϕ and v of the solitons, allowing a proper comparison with theory.

The laser-scanning spectroscopy measurement enables us to extract highly accurate information on the position of the micro-comb lines, which is obtained by beating the micro-comb with a scanning CW laser. Such a CW laser is swept in time and its beating with the micro-comb is read on an oscilloscope, providing the position of the comb lines. The axis of the oscilloscope is calibrated by beating the scanning CW laser itself against a reference comb [10]. The scanning laser is then propagated in a Mach-Zender interferometer to provide accuracy on the frequency below the MHz scale. This approach allows extracting, with high accuracy, the frequency distances between the micro-comb lines.

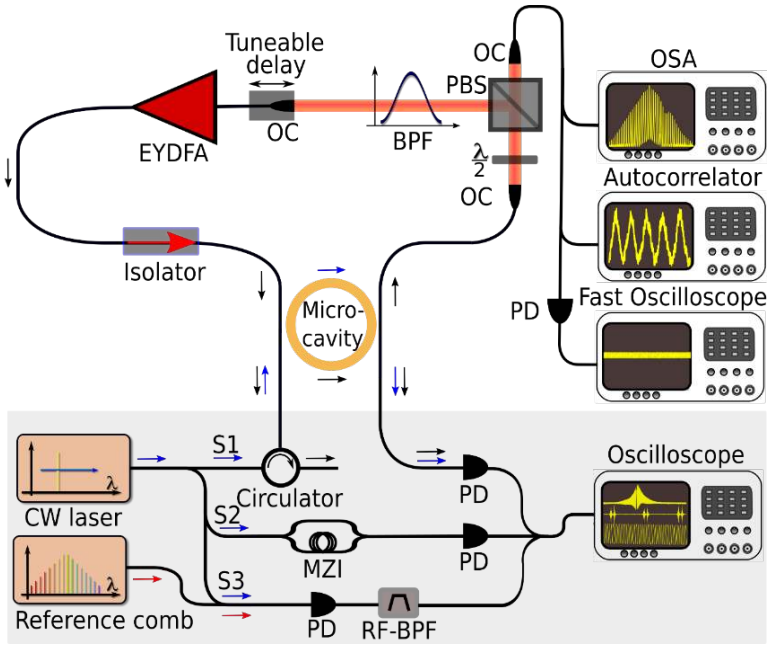

Figure S6. Experimental set-up for micro-comb cavity-solitons' generation and laser-scanning spectroscopy detection of a hot resonator. *The set-up is composed of a nonlinear micro-resonator, an erbium-ytterbium co-doped fibre amplifier (EYDFA), an optical isolator, an optical bandpass filter (BPF), a tuneable delay line, a half-wave plate (λ/2), a polarising beam splitter (PBS) and two optical collimators (OCs). The output signals from the rejection port of the polarising beam splitter were detected with an optical spectrum analyser (OSA), an autocorrelator and a fast photodetector (PD) connected to an oscilloscope. For the laser spectroscopy, a scanning CW laser was split into three signals, S1, S2 and S3. S1 was used to probe the resonances' profile and oscillating micro-comb lines in the hot micro-resonator, while S2 and S3 were simultaneously used to perform frequency calibration of the scanning laser. This was achieved by beating the external CW source with a reference comb (Menlo System, ~ 250 MHz repetition rate). The resulting signal was passed through a radio frequency bandpass filter (RF-BPF) before detection. In this way, it was possible to generate a set of calibration markers with a spacing of ~250 MHz. We created an additional set of finer markers by coupling the signal S3 to an unbalanced Mach-Zender interferometer (MZI) with an FSR of ~7 MHz.*

To gain information on their relative position with respect to the micro-resonator resonances, the CW scanning laser can be coupled directly into the micro-resonator, as in Ref. [10], where this approach was used to get information on the detuning of the micro-comb lines in a standard external pumping configuration. In our case, the scanning CW laser cannot be propagated together with the micro-comb, because it would be also injected in the amplifier, destabilising the system. For this reason, we choose to characterise the small signal backscattered into the micro-resonator, which is expected to be equivalent to the micro-comb oscillation. To achieve this, the CW scanning laser is coupled counterpropagating within the micro-cavity. Figure S6 summarises the setup.

SM 3.2: Role of the detuning of the oscillating lines with respect to the micro-cavity resonance

The intra-cavity laser-scanning spectroscopy measurement allows one to clearly visualise the position of the oscillating lines within the micro-cavity resonance. To get a better understanding of the different system regimes, we performed this measurement also on non-localised states.

Figure S7 reports a set of stable, coherent states with a narrower spectral bandwidth. This kind of states can also be obtained in the same setup used for generating solitons. To reproduce the experimental conditions of Refs [3,11], which employed a narrower passband filter in the setup, we used a passband filter with a 6 nm bandwidth. Similar to Ref [11], we observe states at multiples of the repetition rate, with comb lines from one to four free-spectral ranges apart. Such states have been obtained for different main-cavity lengths, with a similar procedure to Ref. [11]. The autocorrelation shows a very low background which, together with the clean radio-frequency spectrum, indicates the coherence of the state. The intracavity laser spectroscopy of the most powerful, central lines shows that they oscillate in a ***blue-detuned*** position with respect to the micro-cavity resonance.

The solitons reported in Fig. 3 of the main text indicates, conversely, a ***red-detuned*** oscillation.

As discussed in the theoretical section, the stability analysis of the low-energy state provides important information on the type of solutions of the system. Localised states like solitons can be found only in the region in which the background is stable. Solutions originating by the modulational instability of the background, like patterns, are conversely found in the instability region of the background.

The analysis of the zero solution shows that the background is stable only for positive values of the frequency offset Δ, as reported in Fig. S2. Such values correspond to red-detuned frequencies ϕ. This is consistent with the soliton stability region in Fig. S4c and the measurement in Fig. 3. Blue-detuned oscillating lines in general correspond to negative values of the offset frequency Δ. Here, the low-energy state is in general unstable. Type I comb states in Figure S7 and Type II combs (as in Ref. [12], also showing blue-detuned modes) are compatible with the region of existence of patterns originating from the modulational instability of the low-energy state. It is interesting to notice that rolls and Turing patterns are blue-detuned also in the Lugiato-Lefever system for cavities with a positive Kerr coefficient.

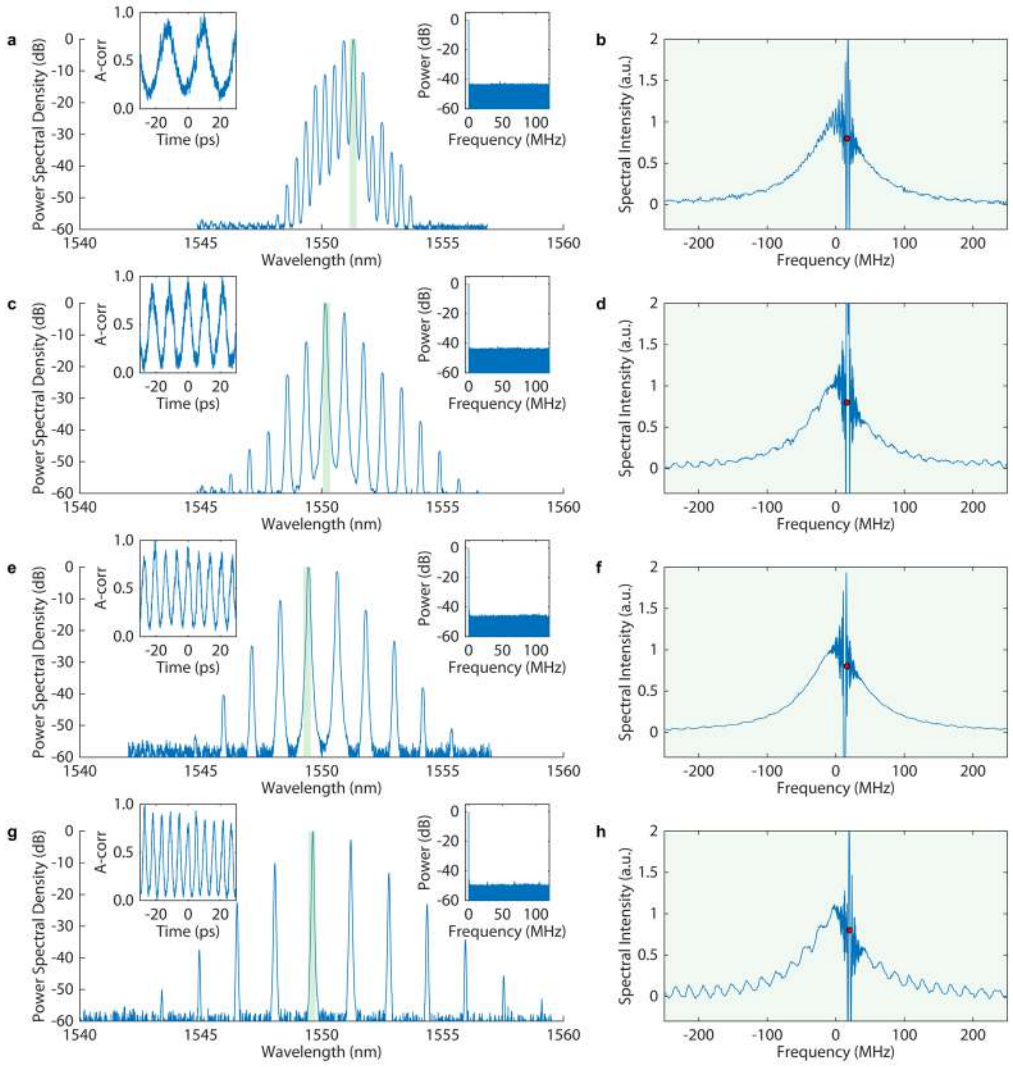

Figure S7. Stable non-localised states. *Coherent state obtained with a setup similar to that of Refs [3, 11] in the main text. States with different FSR are obtained adjusting the cavity length with a similar procedure to that used in Ref. [11].* ***a****. Optical spectrum, autocorrelation (left inset) and radio-frequency spectrum (right inset) of a coherent state at a single micro-ring FSR (approximately 50 GHz) repetition rate.* ***b.*** *Laser scanning spectroscopy measurement for the most powerful spectral line, marked by a green line in panel a. The measurement clearly shows a blue-detuned oscillation.* ***c.*** *and* ***d.*** *Same measurement as in a and b, for a coherent state at the micro-ring FSR twice the repetition rate (approximately 100 GHz).* ***e.*** *and* ***f.*** *Same measurement as a and b, for a coherent state at the micro-ring FSR three-times the repetition rate (approximately 150 GHz).* ***g.*** *and* ***h.*** *Same measurement as a and b, for a coherent state at a four-times the micro-ring FSR (approximately 200 GHz) repetition rate.*

SM3.3: Frequency of perturbation and solitary solutions

Laser scanning spectroscopy allows us to highlight another difference of our system supporting laser cavity solitons with respect to the Lugiato-Lefever system. As observed before, the Lugiato-Lefever equation is a driven system. All the waveforms in the micro-cavity are necessarily locked to the frequency of the input laser, both for solitons and perturbations. Because our system is

homogeneous, conversely, the oscillating frequency is a characteristic of the solution. Solitons and their perturbations have, for this reason, different frequencies.

To better explain this point, here we report a numerical example where we inject into the system a waveform consisting of two or three solitons, as observed for the experiments in Fig. 3 of the main text. We tested the propagation of the calculated solution which matches the experiments, for Δ = 0.49, g = 0.1; for Δ = 0.47, g = 0.14; and finally, for Δ = 0.49, g = 0.11 corresponding to the cases of Fig. 3a, c and e, respectively. The propagations are reported in Fig. S8a, d and g (depicted by false colours in log scale), to better visualise the low energy component of the solution.

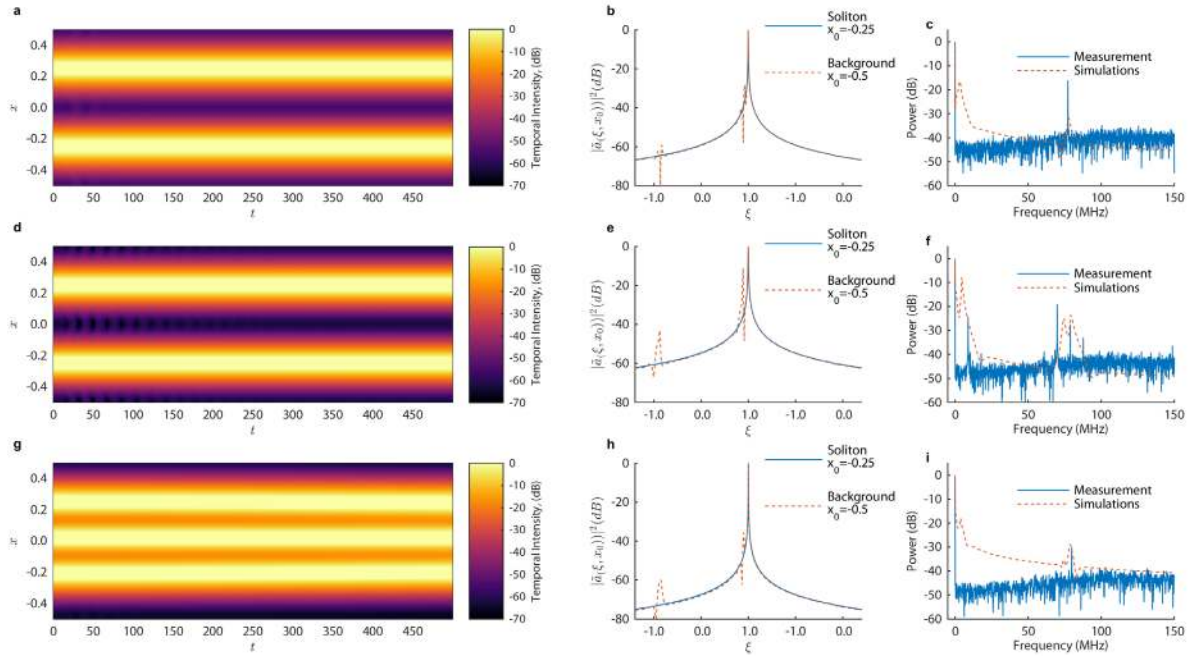

Figure S8. Experimental propagation of soliton pulses. *Here* $\zeta_a = 1.25 \times 10^{-4}$, $\zeta_b = 3.5 \times 10^{-4}$, $\sigma = 1.5 \times 10^{-4}$, $\kappa = 2\pi$. *We have Δ=0.49,* $g = 0.1$*; Δ=0.47,* $g = 0.14$*; and Δ=0.47,* $g = 0.11$ *for a, b, c; d, e, f and g, h, i, respectively.* ***a.*** *Propagation of two soliton pulses, the intensity is displayed in false colours and logarithmic scale to better visualise the spectrum low energy components.* ***b.*** *Slow temporal scale (radio frequency) spectra obtained as the Fourier transform* $\tilde{a}(\xi, x_0) = \int a(t, x_0) e^{-2i\pi\xi t} dt$ *of the propagating solution at the peak (blue,* $x_0 = 0.25$*) and at the tail (orange,* $x_0 = 0$*) of the pulse along the propagating time axis. Note that the spectra are normalised to obtain a maximum at 0 dB. The frequency axis is normalised with respect to the main-cavity FSR.* ***c.*** *Comparison of the experimental RF spectrum (blue) with the background RF spectrum calculated in the simulations as* $\int |a(t, x_0)|^2 e^{-2i\pi\xi t} dt$.

Figure S8b, e and h, report an evaluation of the effective propagating frequency (normalised, as the detuning Δ, against the main-cavity FSR) at the peak ($x = -0.25$, blue line) and at the minimum ($x = -0.5$, orange line) of the propagating intensity. Such a spectrum is calculated as the Fourier transform[2] along the propagating slow axis t at those specific values of x. The frequency axis ξ is centred along the soliton frequency ϕ. This approach reveals the radio

[2] Formally, $\tilde{a}(\xi, x) = \int a(t, x) e^{-2i\pi\xi t} dt$ where ξ is the propagation (slow) axis frequency.

frequency spectrum of the solution and it is also used for the examples of Fig. 1 in the main text, allowing to visualize the presence of unlocked higher-order super-modes.

Here the numerical analysis shows that, in both cases, injecting the stationary states into the system also excites a very small background. The unlocked high-order super-modes are found in such a background, while are absent on the peak of the solitons. Although such a background fades away in propagation because the solitons are stable in such a range of parameters, this analysis shows that the perturbations of the background can coexist with solitary propagation. Very interestingly, this calculation also highlights that the solitary states are very robust to perturbations on their tails.

Because such unlocked components are excited around the cold cavity frequency of the leading order mode ($\xi = -0.05$) and first-order ($\xi = -1$) mode, which are the two dominating super-modes of the interaction, we could find a direct frequency match with the experimentally-observed radio frequency spectrum and laser scanning spectroscopy measurement. Considering that the frequency axis ξ is normalised against the main-cavity FSR $F_b = 77$ MHz, the cold cavity frequency of the leading order mode ($\xi = -0.05$) and first-order ($\xi = -1$) mode correspond to approximately 4 and 77 MHz respectively.

The weak beat-notes in the radio-frequency spectrum can be then attributed to a perturbation of the background. Such a perturbation has frequency components well distinct by the soliton frequency. Specifically, in our experimental cases, we found a perturbation on the first order super-mode (-20dB component at 77 MHz in Fig S8c, f and i). This perturbation is also visible in the laser scanning spectroscopy measurement which reveals a small, blue-detuned frequency found in the central resonances, yet absent in the comb wings of Fig. 3 b, d and f. Fig. S8 f also shows the presence of a perturbation on the leading order super-mode (-20dB component at 6 MHz).

SM3.4: Multiple soliton propagation and input power

Finally, the input average power to the micro-resonator, calculated as $\sum_{q=-N}^{N} \int |b_q(x)|^2 dx$ from the numerical fitting in Fig. 3a and b is 3.1 and 3.8 for the two cases, respectively. Compared to the formation threshold of Lugiato-Lefever bright solitons $8/(3\sqrt{3})\,\kappa^2 = 60.8$, they represent a fractional power of 5.1% and 6.3%, respectively.

References

[1] Haus, H. A. & Huang, W. Coupled-Mode Theory. *Proc. IEEE* 79, 1505–1518 (1991).

[2] Chembo, Y. K. & Menyuk, C. R. Spatiotemporal Lugiato–Lefever formalism for Kerr-comb generation in whispering-gallery-mode resonators. *Phys. Rev. A* 87, 053852 (2013).

[3] Peccianti, M. et al. Demonstration of a stable ultrafast laser based on a nonlinear microcavity. *Nat. Commun.* **3**, 765 (2012).

[4] Conforti, M. & Biancalana, F. Multi-resonant Lugiato–Lefever model. *Opt. Lett.* **42**, 3666 (2017).

[5] Grelu, P. & Akhmediev, N. Dissipative solitons for mode-locked lasers. *Nat. Photonics* **6**, 84–92 (2012).

[6] Malomed, B. A. Solitary pulses in linearly coupled Ginzburg-Landau equations. *Chaos* **17**, 037117 (2007).

[7] Scroggie, A.J., Firth, W.J. & Oppo, G.-L. Cavity-soliton laser with frequency selective feedback, *Phys. Rev. A* **80**, 013829 (2009).

[8] Lugiato, L. A., Prati, F. & Brambilla, M. *Nonlinear Optical Systems*. (Cambridge University Press, 2015).

[9] Rankin, J., Avitabile, D., Baladron, J., Faye, G. & Lloyd, D. J. B. Continuation of Localized Coherent Structures in Nonlocal Neural Field Equations. *SIAM J. Sci. Comput.* **36**, B70 (2013).

[10] Del'Haye, P., Arcizet, O., Gorodetsky, M. L., Holzwarth, R. & Kippenberg, T. J. Frequency comb assisted diode laser spectroscopy for measurement of microcavity dispersion. *Nat. Photonics* **3**, 529–533 (2009).

[11] Wang, W. et al. Repetition rate Multiplication pulsed laser source based on a microring resonator. *ACS Photon.* **4**, 1677–1683 (2017).

[12] Bao, H. *et al.* Type-II micro-comb generation in a filter-driven four wave mixing laser. *Photonics Res.* **6,** B67-B73 (2018).

Appendix

Table 1: Quantities Used in the Full Model

Name	Symbol	Units or Values
Coordinates	T, X	[s], [m]
Fields	A, B	$[\sqrt{\mathrm{W}}]$
Periods, FSRs, Length and velocities	$T_a = F_a^{-1} = L_a v_a^{-1}$, $T_b = F_b^{-1} = v_b L_b^{-1}$ $F_a = (M - \delta)F_b$.	$F_a = 48.9\mathrm{GHz}, F_b = 77\mathrm{MHz}$, $M \approx \frac{F_a}{F_b} = 635$
Dispersions	β_a, β_b	$\beta_a = -20\mathrm{ps}^2\mathrm{km}^{-1}$, $\beta_b = -60\mathrm{ps}^2\mathrm{km}^{-1}$
Coupling constant	$\theta = \pi\, \Delta F_A T_a$	$\Delta F_A = 150\mathrm{MHz}$, linewidth
Gain Bandwidth	ΔF_F	$\Delta F_F = 650$ GHz
Gain	G	$[\mathrm{m}^{-1}]$
Kerr Waveguide Coefficient	γ	$[\mathrm{m}^{-1}\mathrm{W}^{-2}]$

Table 2: Conversions between the Full Model and Normalised Model

Name	Symbol	Value
Time Coordinate	$t = \frac{T}{T_b}$	-
Space Coordinate	$x = \frac{X}{L_a} - \frac{T}{T_b}$	-
Micro-Cavity Field	$a\,(t,x) = A(T,X)\sqrt{\gamma T_b v_a}$	-
Gain-Cavity Field	$b_q\,(t,x) = B_q(T,X)T_b\sqrt{\frac{\gamma v_a}{T_a}}$	-
Gain	$g = GL_b$	$0 < g < 1$
Dispersion ring	$\zeta_a = -\frac{T_b v_a \beta_a}{T_a^2}$	0.000124
Dispersion fibre	$\zeta_b = -\frac{T_b v_b \beta_b}{T_a^2}$	0.000372
Gain dispersion	$\sigma = (2\pi T_a \Delta F_F)^{-2}$	0.000143
Coupling Constant	$\kappa = \theta F_a T_b = \pi\, \Delta F_A T_b$	$2\pi \approx 6.12$